



Review

A Review of Bifunctional Catalysts for Zinc-Air Batteries

Nguyen Huu Huy Phuc^{1,2,3,*}, Tran Anh Tu^{1,2,3}, Luu Cam Loc^{2,4,5}, Cao Xuan Viet^{1,2}, Pham Thi Thuy Phuong⁵, Nguyen Tri⁵ and Le Van Thang^{1,2,3}

¹ Faculty of Materials Technology, Ho Chi Minh City University of Technology (HCMUT), 268 Ly Thuong Kiet Str., Dist. 10, Ho Chi Minh City 70000, Vietnam

² Vietnam National University Ho Chi Minh City, Linh Trung Ward, Thu Duc Dist., Ho Chi Minh City 70000, Vietnam

³ VNU-HCM Key Laboratory for Material Technologies, Ho Chi Minh City University of Technology (HCMUT), 268 Ly Thuong Kiet Str., Dist. 10, Ho Chi Minh City 70000, Vietnam

⁴ Faculty of Chemical Engineering, Ho Chi Minh City University of Technology (HCMUT), 268 Ly Thuong Kiet Str., Dist. 10, Ho Chi Minh City 70000, Vietnam

⁵ Institute of Chemical Technology, Vietnam Academy of Science and Technology, Dist. 12, Ho Chi Minh City 70000, Vietnam

* Correspondence: nhphuc@hcmut.edu.vn

Abstract: Zinc–air batteries are promising candidates as stationary power sources because of their high specific energy density, high volumetric energy density, environmental friendliness, and low cost. The oxygen-related reactions at the air electrode are kinetically slow; thus, the air electrode integrated with an oxygen electrocatalyst is the most critical component, and inevitably determines the performance of a Zn–air battery. The aim of this paper was to document progress in researching bifunctional catalysts for Zn–air batteries. The catalysts are divided into several categories: noble metal, metal nanoparticle (single and bimetallic), multicomponent nanoparticle, metal chalcogenide, metal oxide, layered double hydroxide, and non-metal materials. Finally, the battery performance is compared and discussed.

Keywords: zinc–air battery; bifunctional catalysts; oxygen-related reactions; oxygen-related catalysts



Citation: Phuc, N.H.H.; Anh Tu, T.; Cam Loc, L.; Xuan Viet, C.; Thi Thuy Phuong, P.; Tri, N.; Van Thang, L. A Review of Bifunctional Catalysts for Zinc-Air Batteries. *Nanoenergy Adv.* **2023**, *3*, 13–47. <https://doi.org/10.3390/nanoenergyadv3010003>

Academic Editors: Kwang-Sun Ryu and Ya Yang

Received: 23 October 2022

Revised: 6 January 2023

Accepted: 19 January 2023

Published: 2 February 2023



Copyright: © 2023 by the authors. Licensee MDPI, Basel, Switzerland. This article is an open access article distributed under the terms and conditions of the Creative Commons Attribution (CC BY) license (<https://creativecommons.org/licenses/by/4.0/>).

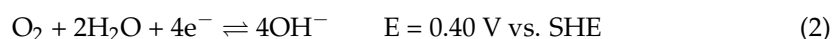
1. Introduction

Rechargeable zinc–air batteries are a century-old technology that have been revived recently because of their high specific energy density, volumetric energy density, environmental friendliness, and low cost [1,2]. The installation cost and levelized cost of energy (LCOE, the price for generating energy) are cheaper compared to revival technologies (lead–acid and Na/S), therefore zinc–air technology is currently being considered as a candidate for grid application. A summary of the installation cost and LCOE of zinc–air, lead–acid, and Na/S batteries is provided in Table 1. Nowadays, many companies are investing their efforts in developing and applying zinc–air batteries, including Urban Electric Power, NantEnergy (formerly Fluidic Energy), EOS Energy Storage, and ZincNyx Energy Solutions [3,4].

Table 1. Summary of installation cost and LCOE of zinc–air, lead–acid, and Na/S batteries [5].

		Installation Cost (\$/kW)	LCOE \$/MWh	LCOE \$/kW yr
Zn-Air	50 MW/6 h	3200	160	355
	1 MW/6 h	3900	200	440
Lead-Acid	50 MW/5 h	3800	220	410
	50 MW/6 h	5780	295	645
Na/S	1 MW/7.2 h	6100	280	~735

A zinc–air battery (ZAB) is typically composed of an air electrode, electrolyte, separator, and zinc electrode. Electrons are released from the zinc electrode and travel through an external load to the air electrode, and Zn^{2+} is generated simultaneously. The Zn^{2+} then reacts with OH^- in the electrolyte to form $[\text{Zn}(\text{OH})_4]^{2-}$ ions, which then decompose to insoluble ZnO at their supersaturated concentration (Reaction (1)). At the air electrode, OH^- ions are generated from the reaction between oxygen, the water in the electrolyte, and electrons on the catalyst surface (Reaction (2)). Then, the generated OH^- ions further travel to the zinc electrode. In the charging process, reverse reactions occur at the electrodes.



The oxygen-related reactions at the air electrode are kinetically slow. Thus, electrocatalysts are employed in the air electrode. The catalyst used in ZABs needs to have suitable oxygen reduction reaction (ORR) and oxygen evolution reaction (OER) activity. Platinum is the best catalyst for the ORR, but it has poor activity in the OER [6]. Ruthenium oxide is the best catalyst for the OER, but its activity in the ORR is poor [7]. On the other hand, iridium and its oxide possess high activity in the ORR and OER, respectively [8]. Therefore, Pt has been combined with either ruthenium oxide or iridium oxide to form bifunctional catalysts which are highly active in the ORR and OER [9–11]. However, the concentrated alkaline solution used in ZABs could hinder the properties of Pt-based catalysts due to the adsorption of OH moiety on the catalyst's active sites [12]. Therefore, efficient bifunctional catalysts are in high demand for the air electrode to improve battery performance.

The main challenge of ORR/OER bifunctional electrochemical catalysts is that the requirements of the active sites of ORR and OER are different. Therefore, finding suitable active materials and properly tuning their intrinsic activity is critical to achieve good performance in both reactions. The design of these catalysts should focus on finding active materials with high intrinsic bifunctional activity and favourable structures to completely enhance the electrocatalyst performance. The bifunctional catalysts for ZABs can be made of noble metal, transitional metal and their oxide, nitride, carbide, chalcogenide, or non-metal materials. Finding those that exhibit high activity and ease of preparation and are environmentally friendly and inexpensive is still a challenge in accomplishing commercialized ZABs. This review aims to summarize the process of finding materials and structures for bifunctional catalysts for use in ZABs. The catalysts are divided into several categories: noble metal, metal nanoparticle (single and bimetallic), multicomponent nanoparticle, metal chalcogenide, metal oxide, layered double hydroxide, and non-metal materials. Finally, the battery performance is compared and discussed.

2. Noble Metals as Advanced Bifunctional Catalysts in Zn–Air Batteries

Carbon-supported Pt and Ir are two well-known catalysts for ORR and OER, but neither can serve as a bifunctional catalyst. The oxidation of carbon occurs at low potential (about 0.207 V vs. RHE at 25 °C), thus the corrosion of carbon is the major issue of catalyst failure under oxygen evolution conditions [13,14]. Nanoparticle Fe_3Pt , as an ORR catalyst, supported on porous nickel–iron nitride (Ni_3FeN), as an OER catalyst, was reported to be an excellent bifunctional catalyst [15]. Its properties surpassed those of the conventional ORR catalyst Pt/C and OER catalyst Ir/C. Linear sweep voltammetry (LSV) of the ORR showed that the onset potential of the catalysts was reduced in the following sequence: $\text{Fe}_3\text{Pt}/\text{Ni}_3\text{FeN} > \text{Fe}_3\text{Pt}/\text{C} > \text{Pt}/\text{C} > \text{Ni}_3\text{FeN}$. In the mixed kinetic–diffusion region, the half-wave potential ($E_{1/2}$) of $\text{Fe}_3\text{Pt}/\text{Ni}_3\text{FeN}$ exhibited the most positive value (0.93 V), which meant that the ORR occurred on the surface of $\text{Fe}_3\text{Pt}/\text{Ni}_3\text{FeN}$ more easily than on other catalysts. $\text{Fe}_3\text{Pt}/\text{Ni}_3\text{FeN}$ also demonstrated better OER activity with lower potential and higher current density than Ni_3FeN , Pt/C, and Ir/C. Accelerated durability tests proved $\text{Fe}_3\text{Pt}/\text{Ni}_3\text{FeN}$, showing that its mass loss was about 6.3% after 5000 ORR potential cycles

and 5.2% after 1000 OER potential cycles; for Pt/C and Ir/C, the values were 20.4 and 22.1%, respectively. Instead of forming an Fe–Pt alloy, their atoms were embedded into nitrogen-doped carbon (PtFeNC) to generate a novel catalyst for ORR [16]. High-onset and half-wave potentials of 1.05 and 0.895 V, respectively, were observed from LSV. The DFT calculation showed that O₂ bond breaking on Pt and Fe single-atom sites of PtFeNC was the origin of its good ORR performance. The E_{1/2} value was lower for PtFeNC than for Fe₃Pt/C and Fe₃Pt/Ni₃FeN (Table 2), even though their onset potentials were similar. The difference in E_{1/2} values proved that the oxygen reduction rate on the PtFeNC surface was slower compared to Fe₃Pt/C and Fe₃Pt/Ni₃FeN. Due to the low activity in OER, this catalyst was only employed for primary ZABs. Since IrO₂ is a catalyst for OER, its mixture with PtFeNC (1:1 weight ratio) showed bifunctional catalytic properties [9].

An integrated catalyst consisting of Co(OH)₂/CoPt/N–CN with a weight ratio of Co(OH)₂:N–CN:Co:Pt of about 45:45:0.77:9.23 was also able to facilitate both ORR and OER for ZABs [17]. SEM and TEM results showed that CoPt nanoparticles and Co(OH)₂ nanosheets attached to the surface of N–CN (nitrogen-doped porous carbon nanosheets) and Co(OH)₂ nanosheets also randomly covered CoPt nanoparticles. This hierarchical structure seemed appropriate for bifunctional catalytic properties (Figure 1a–c). Co(OH)₂/CoPt/N–CN exhibited an onset potential of 0.97 V and an E_{1/2} of about 0.83 V, as determined by the LSV of ORR. In the OER, an overpotential of 0.32 V was required to obtain a current density of 10 mA cm^{−2}. The electron transfer number was about 3.81–3.95 in the voltage range of 0.8–0.2 V, comparable with Pt/C catalyst. In another study, F-doped CoPt alloy (SA–PtCoF) was deposited onto Ni foam and its bifunctional catalytic properties were investigated [18]. The atomic Pt in the alloy was stabilized with fluoride doping because the interstitial F atom could weaken the Co–Pt bond to form Pt atoms. This unique atomic structure resulted in an E_{1/2} of 0.88 V, with an onset potential of 0.95 V. An ideal electron transfer number of 4.0 was obtained in the voltage range of 0.75–0.55 V with LSV of ORR. These data prove that SA–PtCoF had better ORR capability than Co(OH)₂/CoPt/N–CN. In addition, a small overpotential of 0.308 V was needed to acquire an OER current density of 10 mA cm^{−2} with a Tafel slope of 68 mV dec^{−1}, which was also superior to the results obtained from Co(OH)₂/CoPt/N–CN of 0.32 V and 73.4 mV dec^{−1}.

Pt nanoparticles decorated on CoFe₂O₄ hollow spheres also displayed good performance as a bifunctional catalyst for ZABs (Figure 1d) [19]. TEM and HRTEM proved the formation of 100–200 nm CoFe₂O₄ hollow spheres with 3–5 nm Pt particles on their surface. XPS measurement revealed that Pt mainly existed as a zero-valence state on the CoFe₂O₄ surface. The onset potential (E_{onset}) and half-wave (E_{1/2}) potential derived from LSV of ORR were 1.01 and 0.72 V (Figure 1e,f). Despite the high E_{onset}, the low E_{1/2} value illustrates the slow reaction rate on Pt/CoFe₂O₄ in the kinetic-diffusion region compared with the catalysts mentioned earlier. The overpotential to generate 10 mA cm^{−2} of OER current density was 0.28 V, and the Tafel slope was 88 mV dec^{−1}. The lower overvoltage and higher Tafel slope value compared with those of Co(OH)₂/CoPt/N–CN and SA–PtCoF might have originated from the slow rate of the Pt–OH + OH[−] ⇌ Pt–O + H₂O + e[−] reaction that occurred on the Pt nanoparticle surface [20]. Pt nanoparticles supported on Zn nanoplate-decorated Ti mesh were also employed as a catalyst for ZABs [21]. The Pt particle size was about 3–6 nm, similar to Pt/CoFe₂O₄. However, the electrochemical properties of this catalyst were obtained in phosphate-buffered solution (PBS), so it was difficult to compare the values with those acquired in 0.1 M KOH of Pt/CoFe₂O₄.

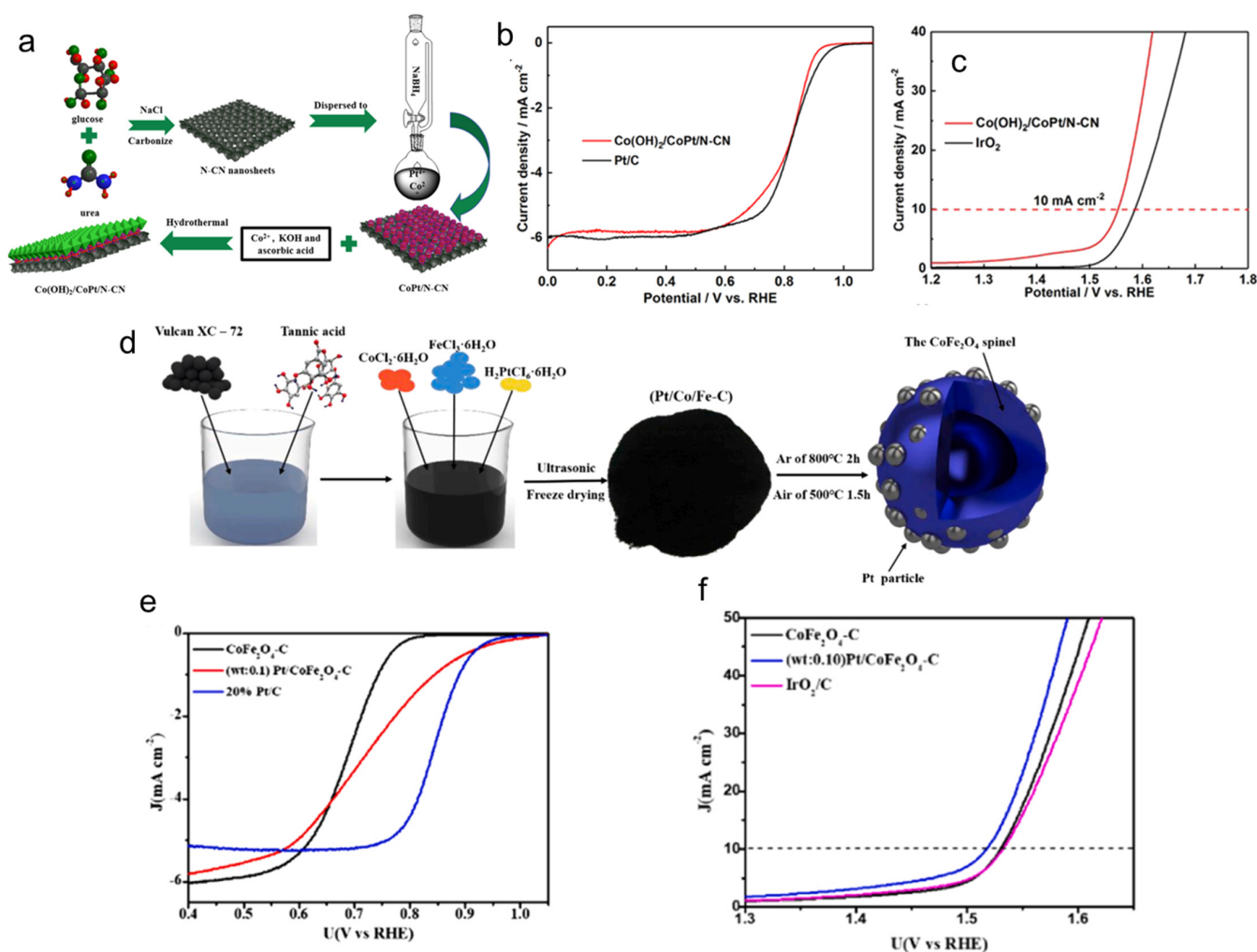


Figure 1. Typical preparation procedure and oxygen-related reaction performance of Co(OH)₂/CoPt/N-CN and SA-PtCoF. (a) Schematic of preparation of Co(OH)₂/CoPt/N-CN composite. (b,c) ORR and OER performance, respectively, of Co(OH)₂/CoPt/N-CN. Reproduced from [17], copyright 2019, Chemical Society of America. (d) Schematic illustration of fabrication process for Pt/CoFe₂O₄-C. (e,f) ORR and OER performance, respectively, of Pt/CoFe₂O₄-C. Reproduced from [19], copyright 2021, Elsevier.

Ag has also been employed as a bifunctional catalyst for ZABs because it is cheaper than Pt and Au and expresses excellent electronic conductivity. In one study, an Ag nanoparticle decorated LaMnO₃ nanorod supported on reduced graphene oxide (Ag/LMO-NR/RGO) was prepared by hydrothermal synthesis of LMO-NR/RGO followed by Ag nanoparticle deposition [22]. Good contacts inside the Ag/LMO-NR/RGO were formed during synthesis, which facilitated the ORR and OER for the ZAB. E_{onset} and $E_{1/2}$ values of ORR were 0.9186 and 0.6906 V, which were better than those of LMO-NR/RGO, 0.8306 and 0.6666 V. In the voltage range of 0.6–0.2 V, the electron transfer number of Ag/LMO-NR/RGO was 3.85–4.0, while that of LMO-NR/RGO was 3.60–4.0. These values prove that Ag nanoparticles enhanced the oxygen reduction reaction and thus reduced the formation of H₂O₂. In order to produce a current density of 10 mA cm⁻², an overpotential of about 0.49 V was required, which was about 0.1 V less than the value for LMO-NR/RGO. Dendritic Ag-Cu polycrystalline deposited on Ni foam (Ag-Cu/Ni) was prepared by galvanic displacement and showed good catalytic ability in ORR and OER [23]. A typical polycrystalline structure of the catalysts was observed. In addition, the fast Fourier transform (FFT) image showed that Ag and Cu crystals were in a relative epithelial relationship in the parallel direction. The E_{onset} value of the catalyst was about 0.801 V

(vs. RHE), and $E_{1/2}$ was about 0.691 V (vs. RHE). This catalyst, surprisingly, produced 10 mA cm^{-2} of OER current density with a slight overvoltage of about 0.27 V (vs. RHE). Ag–Cu metallic glass (MG) and nanocrystal (NC) were decorated on Ni foam by pulse laser deposition (MG) and subsequently annealed in a vacuum chamber at $300 \text{ }^\circ\text{C}$ for 2 h [24]. The Ag–CuMG exhibited a more positive $E_{1/2}$ than the Ag–CuNC. The initial value was 0.67 V, which further increased to 0.78 V via an in situ dealloying process. However, Ag–CuMG exhibited poor catalytic activity in the oxygen reduction reaction, since it required an overpotential of 0.57 V to generate a current density of 10 mA cm^{-2} . The results from Ag/LMO–NR/RGO, Ag–Cu/Ni, and Ag–CuMG/Ni indicated that Ag–Cu nanocrystal or metallic glass outperformed Ag/LMO–NR/RGO in both ORR and OER capability.

Ruthenium oxide exhibited excellent catalytic activity in OER, but its performance in ORR was limited due to sluggish kinetics [8]. Binary Ru–Sn oxide solid solutions prepared by the hydrothermal method demonstrated excellent ability in both OER and ORR [25]. Among the $(100 - x)\text{Ru}-x\text{Sn}$ oxides, those with $x = 30$ and 70 were better in both OER and ORR. The electron transfer number in ORR was 3.78 and 3.8 with $x = 30$ and 70 , respectively, which agreed with the values obtained with RuO_2 , Pt/RuO₂, and Pt/C [9,25]. The E_{onset} and $E_{1/2}$ values of 70Ru–30Sn and 30Ru–70Sn oxides were comparable to those of Pt/C and RuO₂ catalysts. Doping RuO₂ with 30% SnO₂ boosted its OER ability. The OER ability increased in the following order: Pt/C < Ru_{0.3}Sn_{0.7}O₂ < RuO₂ < Ru_{0.7}Sn_{0.3}O₂. A small overvoltage of 0.24 V was enough to generate an OER current density of 10 mA cm^{-2} .

In short, Pt, Ag, and RuO₂ exhibit better catalytic capability in their atomic form better than their nanoparticle form. Pt atoms could be individually embedded in the carbon matrix. The formation of metallic alloys with transition metals (Fe, Co, Cu) stabilize Pt and Ag at the atomic level and thus enhance catalytic activity and stability. In addition, the solid solution formation also enhances the activity of RuO₂ in both ORR and OER.

3. N-Doped Carbonaceous (NC) Materials as Advanced Bifunctional Catalysts in Zn–Air Batteries

Recent efforts to replace Pt-based catalysts lead to the discovery of ORR active nitrogen-doped carbon nanotubes [26]. Since then, researchers have reported different types of carbon-based materials that were found to be active in ORR and OER. Carbon-based materials can be doped with nitrogen and sulfur, boron, phosphorus, hydrogen, or metallic atoms for alkaline ZAB application [27–31].

Cai et al. prepared free-standing vertically aligned nitrogen-doped carbon nanotubes supported by graphene foam (N–VA–CNT/GF) using a multistep process [32]. Structural analysis revealed nitrogen atoms located in the sidewalls of CNTs and carbon fragments on CNT sidewalls. There were four types of nitrogen atoms in the N–VA–CNT/GF composite: pyridinic N, pyrrolic N, graphitic N, and oxidized N. The interconversion of ring-opening of the cyclic C–N bond, which contained pyridinic N and graphitic N, could promote proton transfer, thus improving the ORR activity of N-doped carbon-based materials [33]. Quadripyridinic N also exhibited activity in both ORR and OER, as determined by theoretical calculation and experiment results, and the insertion of pyridinic N into rGO (NDG–800) produced a structure with a large number of defects, thus enhancing its catalytic activity [34]. The NDG–800 catalysts showed exceptional ORR activity, with E_{onset} of 0.98 V and $E_{1/2}$ of 0.85 V vs. RHE. The limited current density was 5.6 mA cm^{-2} . In the OER, an overpotential of 0.45 V was needed to generate a current density of 10 mA cm^{-2} ($E_{j=10}$) with a Tafel slope of 132 mV dec^{-1} . The ORR performance of NDG–800 was comparable with Pt/C, but its OER capability was still far from that of RuO₂/C. A silk-derived defect-rich and nitrogen-doped nanocarbon (SilkNC/KB) was produced by sintering porous Ketjenblack carbon impregnated with silk fibroin in an Ar/H₂ atmosphere and used as a catalyst in the ZAB air electrode [35]. Moderate ORR performance was observed, with E_{onset} and $E_{1/2}$ of 0.94 and 0.764 V, respectively. The $E_{j=10}$ of this catalyst was extremely large, about 0.74 V. Thus, the performance of SilkNC/KB lagged behind that of Pt/C and IrO₂ in 0.1 M KOH solution. Nitrogen-doped porous carbon coated on carbon nanofiber (NPC@CNF) was

prepared by thermal treatment of ZIF-8@BC (bacterial cellulose) at different temperatures under an N_2 atmosphere [36]. The 3D design and flawless contact between NPS and CNF enabled mass transfer for oxygen-related reactions (Figure 2). NPC@CNF-950 (calcinated at 950 °C) displayed good ORR activity, with E_{onset} of 0.99 V and $E_{1/2}$ of 0.88 V. $E_{j=10}$ was 0.47 V, and the calculated Tafel slope was about 132 mV dec^{-1} . The electrocatalytic results of the electrode using NPC@CNF-950 were similar to those of NDG-800 and slightly lower than that of Ni_3FeN [15,34].

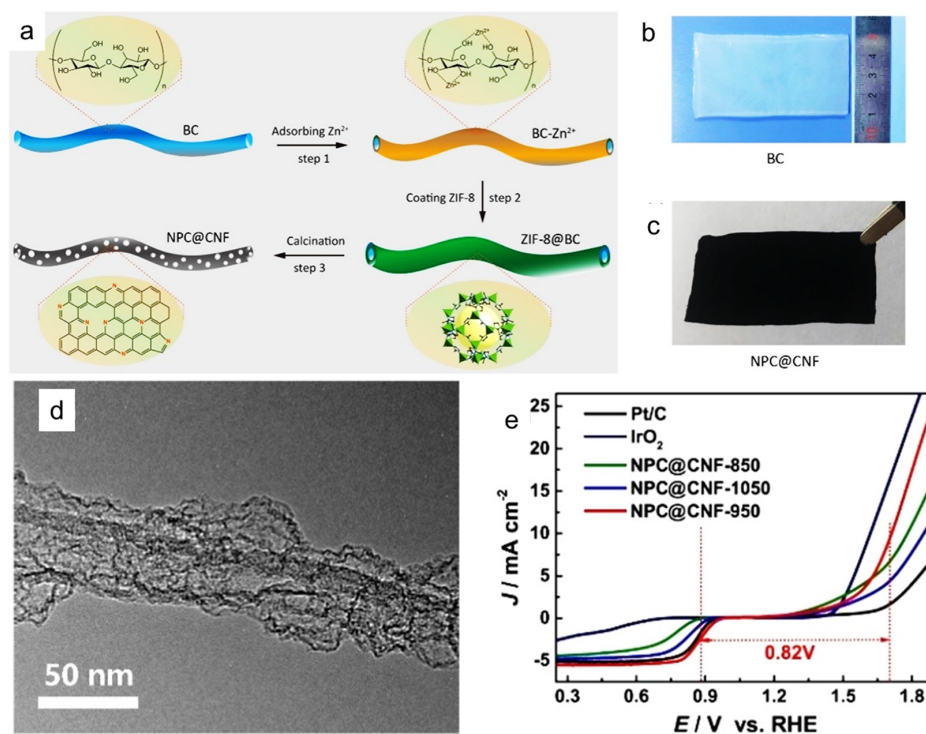


Figure 2. Typical preparation procedure and oxygen-related reaction performance of NPC@CNF. (a) Schematic description of NPC@CNF preparation. (b) Photograph of BC pellicle (size: 4.0 cm \times 8.0 cm) used for preparing NPC@CNF. (c) Photograph of NPC@CNF. (d) TEM images of NPC@CNF-950. (e) LSV curves of different catalysts in ORR and OER at 1600 rpm in the whole ORR/OER region in O_2 -saturated 0.1 M KOH solution. Reproduced from [36], copyright 2021, Wiley-VCH Verlag GmbH & Co.

3.1. Metal-Doped NC

Xu et al. prepared a 2D hybrid structure composed of N-doped CNTs grafted on rGO (GNCNTs) by growing a zeolitic imidazolate framework (ZIF-67) on graphene oxide (GO), and subsequently annealing it in an 5% H_2/Ar atmosphere [37]. X-ray photoelectron spectroscopy (XPS) revealed the existence of pyridinic N, pyrrolic N, graphitic N, and $Co-N_x$ on the GNCNT surface. The 2D hybrid structure of GNCNTs exhibited a large specific area and plenty of pyridinic N and $Co-N$ -carbon active species; therefore, it favoured oxygen-related reactions. E_{onset} and $E_{1/2}$ values derived from LSV were 0.92 and 0.85 V versus RHE. A small Tafel slope of 38 mV dec^{-1} proved the effective electron transfer and fast kinetics of ORR. The electron transfer number was about 3.95, and H_2O_2 yield was about 4.5%. The $E_{j=10}$ was about 0.37 V, which was comparable with Fe_3Pt/Ni_3FeN [15]. Li et al. designed a 3D honeycomb-like porous $Co-N_x-C$ material with high activity in both ORR and OER [38]. They prepared a polyhedral ZIF-67 embedded within orderly assembled polystyrene nanoparticles (PSs), and then removed the PSs to obtain a honeycomb-like product. The obtained ZIF-67 was further calcined in an Ar and NH_3 atmosphere to produce 3D honeycomb-like porous $Co-N_x-C$ material (Honeycomb-600; 600 was the calcination temperature) (Figure 3a,b). The XPS spectra showed that pyridinic N, pyrrolic N, quaternary N, and $Co-N_x$ units existed in the sample (Figure 3c,d). E_{onset} and $E_{1/2}$

values were 0.901, and 0.837 V (Figure 3e,f). The calculated electron transfer number was 3.8, which indicated a four-electron ORR mechanism occurring on Honeycomb-600. The $E_{j=10}$ was 0.38 V, with a small Tafel slope of 85.9 mV dec⁻¹. The results of OER proved the superiority of 3D Honeycomb-600 catalytic activity compared with 2D GNCNT. The 3D structure and high N loading were the source of its excellent catalytic performance.

Multicomponent Co/N/O-doped graphene with atomically dispersed Co-N_x-C active sites (NGM Co) were also reported to function as an air cathode for ZAB [39]. Besides pyridinic N, pyrrolic N, graphitic N, and oxidized N, chemisorbed N was the new feature of NGM-Co compared with the other catalysts, GNCNT and Honeycomb-600. Co-N_x-C was the main Co-containing moiety, and metallic Co was absent in NGM-Co. To clarify the role of Co-N_x-C in the ORR and OER, an NGM catalyst without Co was prepared, and its electrocatalytic activity was investigated. The $E_{1/2}$ value of NGM-Co was about 50 mV, more positive than NGM, and the limiting current density of NGM-Co was also larger than that of NGM. Significantly, the Tafel slope of NGM-Co and NGM was 58 and 119 mV dec⁻¹, respectively. NGM-Co had better ORR activity than NGM, but the OER performance was similar for both catalysts. Therefore, Co-N_x-C plays an essential role in ORR activity, and nitrogen-doped carbonaceous materials are OER active. Li et al. synthesized a Co and N dual-doped carbon catalyst by calcinating ZIF-67 [40]. The resulting catalyst had both Co-N_x-C moieties and metallic Co particles in its structure. In a different attempt, Liu et al. proposed a Co/N co-doped carbon catalyst with a controllable metal vacancy ratio for ZAB air cathodes [41]. The catalyst with a metal vacancy (E-CoSA/N/C) was derived from intrinsic CoSA/N/C by etching with H₂SO₄/H₂O₂ solution. The XPS analysis showed the presence of Co³⁺, Co²⁺, and five types of N structures in CoSA/N/C and E-CoSA/N/C. The Co-N-C species decreased, and pyridinic N increased along with the etching degree. E-CoSA/N/C outperformed CoSA/N/C in oxygen-related reactions. The cyclic stability of the ZAB using E-CoSA/N/C was also better compared to CoSA/N/C, because there was no ZnO deposition on the E-CoSA/N/C air cathode. Thus, the metallic atom vacancy might play a vital role in the catalytic activity of dual-doped metal-nitrogen carbonaceous materials.

The Fe-N_x sites exhibiting catalytic activity in oxygen-related reactions were familiar, and high specific area and rich active sites are the key factors for electron transfer and ionic conduction in ORR and OER [42]. Therefore, 3D carbon-based structures containing Fe-N_x active sites have been attracting attention recently. Wang et al. reported a simple method to prepare 3D Fe/N-doped mesoporous graphene (3D Fe/N-G) using polyacrylamide (PAM), NaCl, and hydrated FeCl₃ as the starting materials [43]. The PAM was employed as both N and C precursor. The raw materials were dissolved in deionized water, followed by pyrolysis at 900 °C in an Ar atmosphere. The received materials were washed with 0.5 M H₂SO₄ to remove the NaCl and crystalline iron species, to obtain a 3D mesoporous Fe/N-G catalyst. The final 3D Fe/N-G contained pyridinic N, pyrrolic N, graphitic N, oxidized N, and Fe-N_x in its structure. The calculated electron transfer number was 3.99, which indicated a perfect four-electron ORR mechanism. The $E_{j=10}$ was 0.393 V and the Tafel slope was 71.5 mV dec⁻¹. In another report, Luo et al. synthesized a bifunctional Fe, N co-doped porous carbon nanosheet (Fe-MNC) and investigated its catalytic activity [44]. Fe-MNC catalysis was prepared by sintering a precursor made from an Fe-2, 2'-dipyridyl coordination complex and cornstalk soot. There were five types of N species in the Fe-MNC, similar to the previously mentioned catalysts. The Fe-MNC catalyst exhibited moderate ORR activity, with an E_{onset} of 0.99 V, an $E_{1/2}$ of 0.85 V, and a limited current density of 5.3 mA cm⁻². Its $E_{j=10}$ was 0.348 V and the Tafel slope was 127 mV dec⁻¹. The Tafel slope value was comparable to NDG-800, SilkNC/KB, and NPC@CNF-950 [34-36]. The similarity of Tafel slope values indicates that an OER happened with those catalysts in the same rate-determining step. A catalytic study using 2D Fe, N co-doped graphene revealed that graphitic N and pyridinic N responded to the OER, while Fe-N_x sites were essential in ORR activity [45]. Therefore, developing a preparation method for a catalyst with many highly exposed active sites is crucial to obtaining a suitable catalyst for ZABs. Indeed, there

are many strategies to disperse Fe-N_x moieties inside a carbon skeleton to produce catalysts with good ORR performance. These strategies employ citric acid, polyvinylpyrrolidone (PVP), or 2, 2-bipyrodine to form coordination with Fe ions in the precursor solution to prevent the crystallization of FeC_x in the final product [46–48].

3.2. Non-Metal-Doped NC

Besides metallic atoms, sulphur also enhanced the ORR activity of N-doped carbon-based materials. Ma et al. prepared N and S dual-doped porous carbon material (GSC-900; 900 was the calcination temperature) from bio-waste (garlic stems) using a simple process [49]. The XPS spectrum proved the appearance of N and S as heteroatoms in a carbon skeleton. Pyridinic N, pyrrolic N, graphitic N, and oxidized pyridinic N were found in GSC-900. Two other types of sulphur existed in the sample: C-S-C and C-SO_x-C; the latter was inactive for ORR. The C-S-C species were mainly located at the edge of the carbon layer and formed defects in the carbon structure. The catalysts exhibited reasonable ORR, with an E_{onset} of 0.89 V and E_{1/2} of 0.8 V. The OER data were omitted in the paper, but the stability of the ZAB using GSC-900 as the air cathode showed that this catalyst was also OER active. Using a similar approach, Zhu et al. prepared porous, cheese-like N, S-doped carbonaceous material (CF-K-A, where K is KOH and A is NH₃) from keratin-rich chicken feathers [50]. Three other types of N species, pyridinic N, pyrrolic N, and graphitic N, were detected, while S existed in thiophene and oxidized forms. The high specific surface area with a defect-rich structure seemed to be the main driving force for the high ORR activity of CF-K-A (high E_{1/2} of 0.835) compared with CF-K and CF-A, because it had the most significant specific area but the lowest N and S content among the three samples. In another study, Kim et al. employed bamboo stems as the carbon source to prepare S, N co-doped bamboo carbon (SNBC) [51]. They found that the ORR ability of SNBCs (E_{1/2}) was associated with the mesopore ratio (%) and doping content (wt%). A doping content of about 7.2 wt% and a mesopore ratio of about 0.4% were related to the most positive E_{1/2}, and the effect of the mesopore ratio on E_{1/2} was more clear than that of the doping content. By investigating the electrochemical properties of hierarchical N, S co-doped carbon nanocages, Fan et al. found that C-S-C and pyridinic N in 3D hierarchical sulfur and nitrogen co-doped carbon nanocages (hSNCNCs) improved the OER activity of the catalyst. In contrast, C-S-C, C-SO_x-C, pyridinic N, pyrrolic N, and graphitic N ameliorated the ORR activity (Figure 3g) [52].

Similarly, phosphorous also boosted the oxygen reduction capability of NC materials. P, N dual-doped porous carbon nanospheres (DDPCNs) showed good ORR activity, with an E_{onset} of 0.98 V and E_{1/2} of 0.87 V [53]. Doping of P was associated with an increased pyridinic N ratio, and thus the catalytic activity was enhanced, because the carbon atoms connecting to the pyridinic N were electrocatalytically active [33]. P-O, P-C, and P-C-N were the newly formed bonds in DDPCNs. The kinetic current density of the three samples (N-doped, P-doped, and co-doped) expressed the synergistic effect of co-doping. The E_{onset} and E_{1/2} values also proved that the N, P co-doped sample exhibited better ORR activity than the mono-doped samples. Chen et al. also prepared N, P dual-doped 3D hierarchical porous carbon (NPHC-2) for application as the air cathode in ZAB [54]. Only a small amount of P was successfully incorporated into the carbon skeleton, ≤0.56 atomic %, while N could be loaded up to 2.72 atomic %. Pyridinic N, pyrrolic N, and graphite N were the three types of nitrogen-containing species in NPHC-2. Observation of the phosphorous-containing structure was difficult because of its low loading. P-C and P-O were detected by the high-resolution XPS spectrum of P 2p. The positive effect of dual doping on ORR performance was observed in NPHC-2 when different samples with lower doping were compared in the same study.

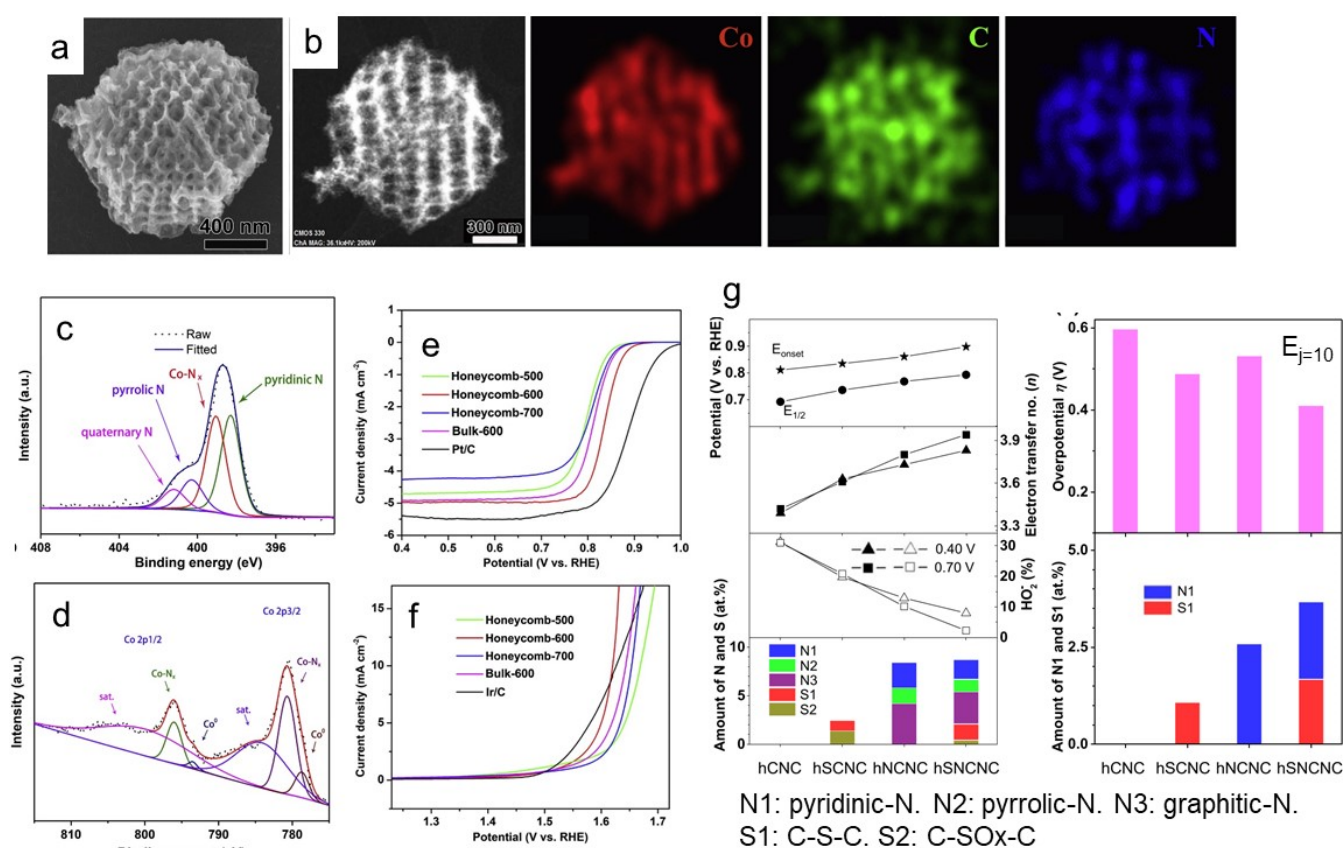


Figure 3. Relationship between the structures and electrochemical properties of typical catalysts. (a) SEM image; (b) energy-dispersive X-ray mapping results; (c,d) N 1s spectrum and Co 2p spectrum; (e,f) ORR and OER LSV curves of Honeycomb-600 (reproduced from [38], copyright 2020, Elsevier); (g) ORR- and OER-related indexes versus amount of highly active N and S sites in hCNC, hSCNC, hNCNC, and hSNCNC (reproduced from [52], copyright 2020).

Nitrogen-doped carbon exhibits good oxygen reduction ability; however, ZABs require a bifunctional catalyst with both OER and ORR ability. The OER catalytic activity of NC could be boosted by either co-doping or mixing it with an OER catalyst. Iron, cobalt, sulfur, and phosphorus enhance oxygen-related reactions when they exist in the NC skeleton in the form of Co-N_x , Fe-N_x , C-S-C , P-O , P-C , or P-C-N .

4. Metallic Nanoparticles as Advanced Bifunctional Catalysts in Zn-Air Batteries

Precious metals such as Pt, Ir, Ru, Ag, and Pd are effective electrocatalysts for ORR and OER, but their high cost and poor cyclic stability are the main drawbacks preventing them from being employed in commercialized ZABs [55,56]. Therefore, transitional metal nanoparticles have been intensively studied to find excellent bifunctional catalysts for ZABs [57–59]. Co, Fe, Cu, Ni, and their metallic alloys have been fabricated in different morphologies and composite structures to examine their catalytic properties in oxygen-related reactions.

4.1. Single Metallic Particles

Co nanoparticles encapsulated in nitrogen-doped carbon nanotubes (Co-N-CNTs) were prepared by high-temperature pyrolysis on a hybrid leaf-like Co/Zn zeolitic imidazolate framework (ZIF) and used as a bifunctional catalyst [60]. The structural analysis results showed that Co-N-C was the active site and was in full contact with the CNT surface. This unique structure was beneficial for enhancing electrode catalyst properties. The high E_{onset} and $E_{1/2}$ values of the LSV curve were 0.97 and 0.90 V vs. RHE, respectively. Those values were comparable with the results from $\text{Fe}_3\text{Pt/C}$ and SA-PtCoF [15,18]. In order to generate

a current density of 10 mA cm^{-2} ($E_{j=10}$), an overpotential of 0.46 V was needed for OER. Calcination of ZIF-67 functionalized electrospun polyacrylonitrile (PAN) nanofibers produced cobalt nanoparticles encapsulated in nitrogen-doped carbon nanofibers (CNCFs), which also served as a bifunctional catalyst [61]. The diffusion-limited current density, E_{onset} , and $E_{1/2}$ of the LSV curve were 4.32 mA cm^{-2} , 0.83, and 0.66 V, respectively. These values are lower than those obtained from Co–N–CNTs [60]. However, $E_{j=10}$ was 0.41 V, which was comparable to the 0.46 V seen on the OER LSV curve of Co–N–CNTs. Figure 4a illustrates the synthesis process of Co@NCNTAs on carbon cloth (CC) substrate. The CC substrate was first immersed in a solution of Co^{2+} and Zn^{2+} in 2-methylimidazole (2-MIM) at room temperature to grow nanosheet arrays for a bimetallic cobalt–zinc zeolitic imidazolate framework (CoZn–ZIF). The Co@NCNTAs were then uniformly formed after calcination of CoZn–ZIF in a dicyandiamide-containing atmosphere (Figure 4b) [62]. Excellent catalytic performance in the ORR and OER was observed on self-supported cobalt-encapsulated nitrogen-doped carbon nanotube arrays (Co@NCNTA-700), with E_{onset} , $E_{1/2}$, and $E_{j=10}$ values of 0.973, 0.861, and 0.28 V, respectively (Figure 4c). Liu et al. recently reported the preparation and catalytic properties of Co nanoparticles encapsulated in nitrogen-doped carbon nanotubes (Co@NC-3) [63]. The values of $E_{1/2}$ and $E_{j=10}$ were 0.816 and 0.49 V. Based on the results of the catalytic study of different Co nanoparticles embedded in carbon nanotube structures, self-supported cobalt-encapsulated nitrogen-doped carbon nanotube arrays (Co@NCNTA-700) were the best, because of the ultimate contact formed among the components of the catalyst due to the particular 3D structure.

Co particles confined within carbon nanotubes anchored on rGO (Co/N–CNTs@rGO) was recently reported as an efficient bifunctional catalyst [64]. This newly developed composite structure enhanced the catalytic properties of Co nanoparticles embedded inside CNTs. The E_{onset} , $E_{1/2}$, and $E_{j=10}$ values were 0.98, 0.88, and 0.381 V, respectively. In another case, a 3D structure of Co nanoislands rooted on Co–N–C nanosheets supported by carbon felts (Co/Co–N–C) was prepared for ORR and OER. The E_{onset} , $E_{1/2}$, and $E_{j=10}$ values were 0.82, 0.68, and 0.47 V, respectively. Co/Co₂N inserted into nitrogen-doped porous carbon (Co@NC-5) was the most updated 3D structure that could catalyse both ORR and OER for ZAB [65]. The E_{onset} , $E_{1/2}$, and $E_{j=10}$ values were 0.95, 0.86, and 0.39 V, respectively. The electron transfer number (3.87–3.92) proved that oxygen reduction occurred on the Co@NC-5 catalysts in a four-electron pathway. The catalytic performance of Co@NC-5 was comparable to that of Co/N–CNTs@rGO and better than that of Co/Co–N–C. The results show that the 3D structure of Co@NC-5 and Co/N–CNTs@rGO facilitated fast mass/electron transfer due to the connections between active catalytic sites and conduction pathways.

4.2. Bimetallic Particles

A single metallic Co nanoparticle could serve as a bifunctional catalyst in ZAB, and a CoFe alloy was also found to be electroactive in ORR and OER [66]. Nitrogen-doped carbon was recognized as an outstanding support for metallic catalysts in the ORR and OER because of the ease of electron transfer from the active sites of the catalyst [67,68]. The combination of CoFe alloy and nitrogen-doped carbon resulted in many other electrocatalysts, and the preparation method played a crucial role in their morphology and catalytic performance [69–71]. Besides the CoFe metallic alloy, a CoNi alloy was also combined with N-doped carbon for application as a bifunctional catalyst [72–74].

Heat treatment of $\text{Co}_3[\text{Fe}(\text{CN})_6]_2(\text{H}_2\text{O})_{17}$ (Co–Fe doped Prussian Blue analogue) at 750 °C led to the formation of core–shell structured FeCo@NC-750 nanoparticles (FeCo@NC-750) (Figure 4d) [75]. In another approach, hollow FeCo alloy nanoparticles inserted into nitrogen-doped carbon nanofibers (h-FeCo alloy/N–CNFs) were prepared by calcination of Co–PBA-containing PAN in an Ar atmosphere [76]. Both FeCo@NC-750 and h-FeCo alloy/N–CNF were highly active in the OER and ORR. Interestingly, their catalytic performance was similar. The E_{onset} , $E_{1/2}$, and $E_{j=10}$ values of FeCo@NC-750 were 0.94, 0.80, and 0.22 V (Figure 4e,f), while the values for the h-FeCo alloy/N–CNF were 0.95,

0.87, and 0.368 V. Tafel slopes derived from OER LSV curves of the nanoparticles and hollow particles were 52 and 62.74 mV dec⁻¹, respectively. The Tafel slopes show that $\text{MOOH} + \text{OH}^- \rightleftharpoons \text{MOO}^- + \text{H}_2\text{O}$ (M is the active catalytic site) determined the overall reaction rate [20].

CoFe nanoparticles attached to the inside wall of nitrogen-doped carbon nanotubes (CoFe@NCNTs) were prepared by thermal decomposition using a precursor containing $\text{Co}(\text{NO}_3)_2$, $\text{Fe}(\text{NO}_3)_3$, and dicyandiamide [77]. This structure prevented FeCo nanoparticles from agglomerating and thus maintained a large surface area to expose active sites, in order to accelerate oxygen-related reactions. The E_{onset} , $E_{1/2}$, and $E_{j=10}$ values of CoFe@NCNTs were 0.95, 0.84, and 0.45 V, respectively. A structure composed of core-shell particles decorated on nitrogen-doped CNTs ($\text{Fe}_{1.2}\text{Co@NC/NCNTs}$) was reported by Li et al. [78]. A precursor formed by self-assembly of cobalt phthalocyanine and iron phthalocyanine on CNTs in the presence of melamine was sintered in an inert atmosphere to produce $\text{Fe}_{1.2}\text{Co@NC/NCNTs}$. The E_{onset} , $E_{1/2}$, and $E_{j=10}$ values of $\text{Fe}_{1.2}\text{Co@NC/NCNTs}$ were 0.842, 0.82, and 0.355 V, respectively. The E_{onset} and $E_{1/2}$ values of CoFe@NCNTs were slightly more positive than those of $\text{Fe}_{1.2}\text{Co@NC/NCNTs}$, but the limited current density was similar in both cases. The Tafel slope of ORR LSV obtained from $\text{Fe}_{1.2}\text{Co@NC/NCNTs}$ was about 52 mV dec⁻¹, smaller than that of CoFe@NCNTs. The Tafel slope of OER LSV obtained from $\text{Fe}_{1.2}\text{Co@NC/NCNTs}$ was about 66 mV dec⁻¹, smaller than that of CoFe@NCNTs (158 mV dec⁻¹). From the Tafel slope of the ORR, it could be concluded that $\text{MO}_2^- + \text{H}_2\text{O} \rightleftharpoons \text{MO}_2\text{H} + \text{OH}^-$ was the rate-determining step of the oxygen-reduction process occurring on $\text{Fe}_{1.2}\text{Co@NC/NCNTs}$ [20]. The high value of 158 mV dec⁻¹ shows that the combination of OH^- and the active catalytic site on CoFe@NCNTs was the rate-determining step of the oxygen evolution process. In contrast, the Tafel slope of OER shows that $\text{MOOH} + \text{OH}^- \rightleftharpoons \text{MOO}^- + \text{H}_2\text{O}$ was kinetically slowest in the case of $\text{Fe}_{1.2}\text{Co@NC/NCNTs}$.

It was also found that Ni-Fe metallic alloy nanoparticles improved the ORR of nitrogen-doped carbon in a ZAB, as Corrigan reported that a composite of hydrous Fe and Ni on NiO thin film could serve as a new electrocatalyst in an alkaline medium [79]. Two other $\text{Ni}_3\text{Fe-NC}$ structures have been reported so far: nanoparticles decorating NC nanosheets and nanoparticles embedded inside NC. The precursors for the preparation of Ni_3Fe nanoparticles-NC nanosheets were inorganic salts of $\text{Ni}^{2+}/\text{Fe}^{2+}$ salts and GO, pyridine, and graphitic C_3N_4 [80–82]. The Ni_3Fe particle size was an essential factor in the OER capability of the bifunctional Ni_3Fe nanoparticles-NC nanosheets because it reflected the number of active sites exposed to electrolytes and air. Ni_3Fe particles of about 1 nm ($\text{Ni}_3\text{Fe/NPG-1}$, where NPG is nitrogen-doped porous graphene) showed superior OER activity compared with bigger particles of ~98 and ~147 nm [81]. Fe-enriched FeNi_3/NC and $\text{Ni}_3\text{Fe/N-C}$ prepared in different studies had an alloy particle size of 10–20 and ~29 nm, respectively [80,82]. The value of the Tafel plot of $\text{Ni}_3\text{Fe/NPG}$ and Fe-enriched FeNi_3/NC was 82 mV dec⁻¹, while that of $\text{Ni}_3\text{Fe/N-C}$ was 58 mV dec⁻¹. Those values prove that the OER occurred on $\text{Ni}_3\text{Fe/NPG}$ and Fe-enriched FeNi_3/NC with the same kinetics. However, the difference between the $E_{j=10}$ of $\text{Ni}_3\text{Fe/NPG-1}$ (0.329 V) and Fe-enriched $\text{Ni}_3\text{Fe/NC}$ (0.36 V) indicates that the electrode using $\text{Ni}_3\text{Fe/NPG-1}$ outperformed the one using Fe-enriched $\text{Ni}_3\text{Fe/NC}$. This advantage originated from the higher alloy loading in $\text{Ni}_3\text{Fe/NPG-1}$ than in Fe-enriched $\text{Ni}_3\text{Fe/NC}$ (2.4 wt%), which is related to the number of exposed active sites for ORR.

Embedding Ni-Fe alloy nanoparticles within the wall of CNTs was another method of constructing the NiFe-NC composite. Jiang et al. created three-dimensional microsphere bifunctional catalyst particles using the encapsulation of NiFe alloy nanoparticles ($\text{Ni}_{0.36}\text{Fe}_{0.64}$) into N-doped carbon nanotubes (NiFe@NCNTs) [83]. The resulting NiFe@NCNT electrocatalyst delivered remarkable performance, with a positive $E_{1/2}$ (0.79 V) for the ORR, and low overpotential and Tafel slope ($E_{j=10} = 0.330$ V, 77 mV dec⁻¹) for the OER. In another attempt, Wang et al. reported the preparation of FeNi alloy nanoparticles inlaid on bamboo-like N-doped carbon nanotube (CNT)-tangled porous carbon fibres

(FeNi/N-CPCF) for ZABs [84]. The as-prepared FeNi/N-CPCF-950 demonstrated an $E_{1/2}$ of 0.867 V for ORR and a low operating potential $E_{j=10}$ of 0.355 V, with a Tafel slope of 67 mV dec^{-1} for OER in 0.1 M KOH. Figure 4g shows the TEM image of an excellent bifunctional catalyst consisting of Ni_3Fe alloy nanoparticles incorporated in heteroatom (N/S)-doped 3D carbon nanotube/graphene nanosheets ($\text{Ni}_3\text{Fe}/\text{N-S-CNTs}$), constructed by Lai et al. [85]. The combination of Ni_3Fe nanoparticles and N-S-CNTs and the abundance of reactive sites made $\text{Ni}_3\text{Fe}/\text{N-S-CNT}$ catalyst exhibit excellent OER performance, with a low $E_{j=10}$ of 215 mV, efficient ORR activity and an $E_{1/2}$ potential of 0.877 V. XPS results (Figure 4h,i) show the peak shift of N 1s and S 2p in the $\text{Ni}_3\text{Fe}/\text{N-S-CNTs}$ compared to N-S-CNTs. The peak's shift of N 1s and S 2p in $\text{Ni}_3\text{Fe}/\text{N-S-CNTs}$ originated from the electronic interaction between Ni_3Fe and N-S-CNTs enhancing the adsorption energy of oxygen, resulting in the synergistic enhancement of OER and ORR catalytic activity.

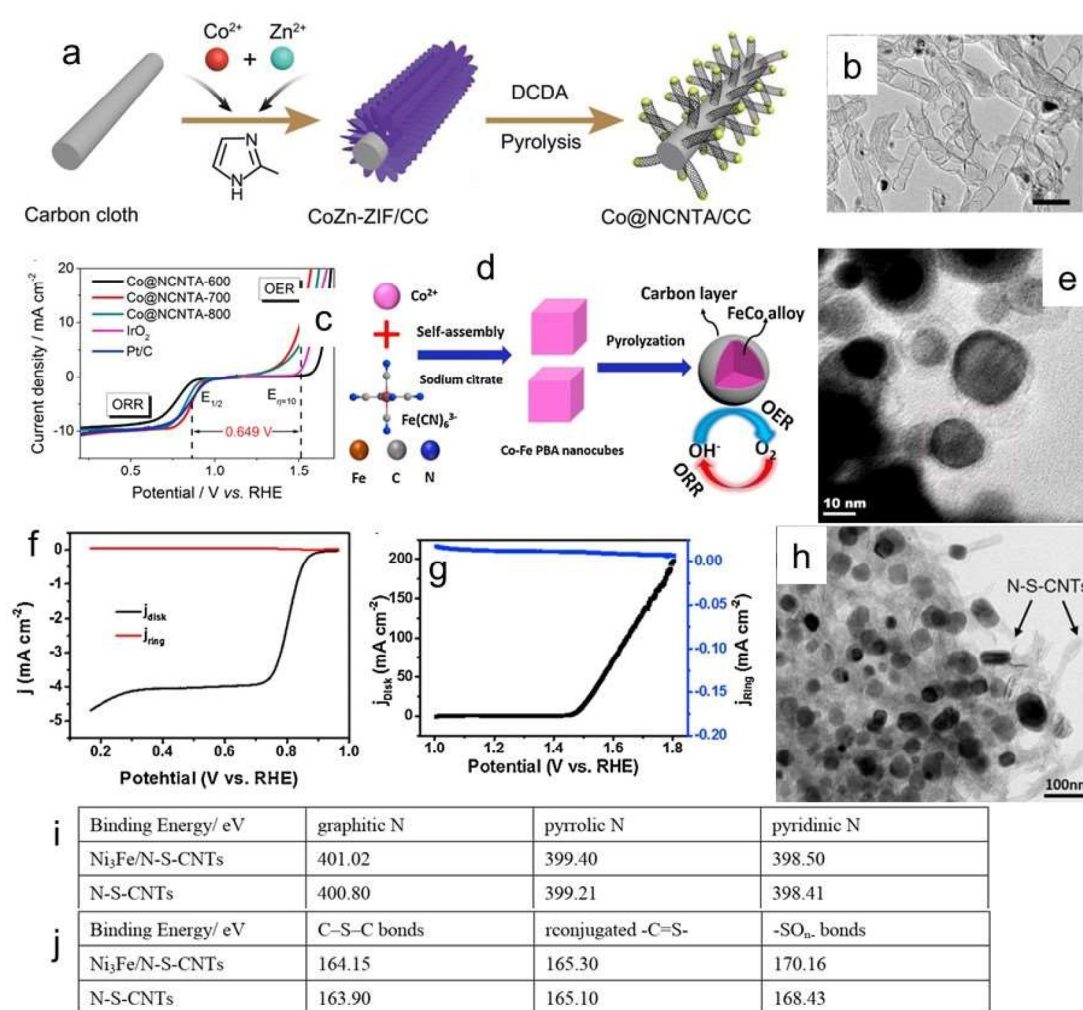


Figure 4. Preparation procedure and oxygen-related reaction performance of Co@NCNTA, FeCo@NC, and FeNi₃@NC. (a) Synthesis process for Co@NCNTA. (b) Low-magnification TEM image. (c) Overall polarization curves of Co@NCNTA-600, Co@NCNTA-700, Co@NCNTA-800, Pt/C, and IrO₂ in 0.1 M KOH solution. Overall electrocatalytic oxygen performance ($\Delta E = E_{j=10} - E_{1/2}$) confirmed by half-wave potential for ORR and potential for OER at 10 mA cm^{-2} . Reproduced from [62], copyright 2019, Wiley-VCH Verlag GmbH & Co. (d) Synthesis of FeCo@NC core-shell nanoparticles. (e) TEM image of FeCo@NC-750; (f,g) Polarization curves of disk and ring current density on an RRDE at the rotating speed of 1500 rpm of FeCo@NC-750. Reproduced from [75], copyright 2016, Elsevier. (h) TEM image of $\text{Ni}_3\text{Fe}/\text{N-S-CNTs}$. (i,j) Statistics of bonding energy measured by XPS. Reproduced from [85], copyright 2018, Chemical Society of America.

The combination of nitrogen-doped carbonaceous materials and metallic nanoparticles produces prominent active catalysts. Co nanoparticles contribute to the ORR ability, while Fe-based nanoparticles improve the OER. Ni₃Fe/N-S-CNTs and FeNi₃@NC exhibit catalytic properties comparable to those of the noble metals' catalysts.

5. Layered Double Hydroxides as Advanced Bifunctional Catalysts in Zn–Air Batteries

Layered double hydroxides (LDHs) are 2D hydrotalcite-like materials whose general formula is known as $[M_{1-x}^{2+}M_x^{3+}(\text{OH})_2]^{x+}(\text{A}^{n-})_{x/n} \cdot m\text{H}_2\text{O}$ [86]. Their excellent redox characteristics are due to the unique structure consisting of incorporated anions, A^{n-} , and hydroxides between large interlayer spaces formed by brucite-like sheets of divalent (M^{2+}) and trivalent (M^{3+}) metal cations [87,88]. In addition, the tuneable composition of LDHs makes their synthesis from metals such as Fe, Co, Ni, Al, Mn, and Zn more flexible and easier [89].

NiFe LDH has attracted extensive interest owing to its outstanding OER performance in alkaline medium [90]. However, its intrinsically poor conductivity and aggregation, as well as limited active sites and stability, limit bulk Ni-based LDH applications in the energy storage and conversion field. Thus, constructing a composite with ORR catalysts using heterostructural engineering is an efficient strategy to achieve active bifunctional electrocatalysts for rechargeable ZABs. An NiFe-LDH-based Janus-type electrode was developed by Wang et al. [91,92]. While the synthesis procedure was the same, the two electrodes were manufactured differently due to a slight difference in the composition of precursors for the ORR active site. Accordingly, MnO_x was anodically electrodeposited from an electrolyte containing manganese sulphate monohydrate, sodium acetate, and sodium dodecyl sulphate, while MnO₂ was formed from sodium sulphate and manganese acetate. Both catalysts demonstrated similar OER catalytic activity compared to NiFe LDH, which surpassed bare MnO₂ and MnO_x. Meanwhile, the high ORR catalytic activity of MnO₂ and MnO_x was maintained due to the unique structure of the Janus-type electrode that allows OER and ORR active sites to work separately without being buried and losing access to the electrolyte.

Zhang et al. prepared NiFe LDH supported on Co-doped carbon nanotube (CNT) by a coprecipitation hydrothermal method (NiFe LDH–CoPc/CNT, where CoPc is cobalt phthalocyanine) [93]. Benefiting from the high specific surface area, good conductivity, and porous structure of CNT, the OER and ORR activity of the NiFe LDH–CoPc/CNT was comparable to that of the NiFe LDH and CoPc components. Qian et al. also reported a Janus-type electrode composed of NiFe LDH nanoplates and nitrogen-doped carbonaceous networks derived from the metal–organic framework (MCN) for rechargeable ZABs [94]. The OER activity of NiFe LDH nanoplates (MCN-LDH-1.5) was significantly enhanced by anchoring them onto MCN via a simple hydrothermal reaction at an optimum ratio. In contrast, no enhancement was observed in the physical mixing of these two materials (MCN-LDH mix-1.5) due to the composite's more vital interaction between MCN and NiFe LDH. However, dispersing NiFe LDH nanoplates onto MCN also prevented them from being buried and losing access to the electrolyte. Therefore, increasing the loading dose of NiFe LDH on MCN decreased OER activity due to an increase in electron transfer resistance. MCN-LDH-1.5 demonstrated an $E_{1/2}$ of 0.826 V for ORR and a moderate operating potential $E_{j=10}$ of 0.44 V with a Tafel slope of 140 mV dec^{−1} for OER in 0.1 M KOH. Chen et al. developed a hybrid hierarchical architecture in which lamellar NiFe LDH was anchored on the surface of cobalt and nitrogen co-doped hierarchical carbon (Co-NC) (Figure 5a,b) [95]. Co nanoparticles with a diameter of about 10 nm were covered at the tip of CNTs (Figure 5c,d). Generally, the cations on the LDH surface are considered the active OER catalytic sites, and the synergistic effect of Ni and Fe ions in the alkaline electrolyte significantly improves OER catalytic activity. The interaction of Ni²⁺ and Fe³⁺ with Co-NC@LDH pulls electron density away from the metal cations, making their Ni 2p and Fe 2p electrons harder to remove. Therefore, peaks of Ni 2p and Fe 2p in Co-NC@LDH shifted about 1–2 eV compared with those of NiFe-LDH, because of NiFe-LDH nanosheets

anchored on the Co-NC@LDH (Figure 5e,f). Protruding ORR active sites from the substrate surface protected them from shielding by NiFe LDH and maintained good mass transfer of reactants, resulting in similar ORR and OER activity in the composite Co-NC@NiFe LDH as compared to its components (Figure 5g).

Co-based materials such as NiCo₂O₄, Co₃O₄, and NiCo₂S₄ were also employed as ORR catalysts and integrated with NiFe LDH to make bifunctional catalysts [96–98]. These composites exhibited enhanced OER and ORR activity compared to the NiFe LDH component due to the tuneable electronic structure and the presence of additional ORR active sites, respectively. In addition, the electron transfer from the outer Fe and Ni species to the inner Co species could generate additional OER active sites and accelerate the OER reaction. Meanwhile, an enhancement in ORR activity was observed in the case of NiCo₂O₄@NiFe LDH and NiCo₂S₄@NiFe LDH due to their unique nanostructure and the synergistic effect of the component materials. Depositing NiFe LDH onto Co₃O₄ nanowires caused a decrease in the valence state of Co ions, resulting in lower ORR activity of Co₃O₄@NiFe LDH composite compared to the Co₃O₄ component. However, the most crucial advantage of making an outer shell NiFe LDH is that it improves the stability of the Co₃O₄@NiFe-LDH, NiCo₂O₄@NiFe LDH, and NiCo₂S₄@NiFe LDH composites by protecting the inner core ORR catalysts from corrosion. Figure 5h shows that NiCo₂S₄@NiFe LDH had cactus-like hollow spheres, in which numerous nanowires and nanosheets constructed a hollow nanostructure. The nanowires (NWs) extended outward from some nanosheets and the surface of NiCo₂S₄ hollow spheres. The Ni 2p XPS spectra of Ni 2p_{3/2} and Ni 2p_{1/2} of Ni²⁺ in NiCo₂S₄@NiFe LDH exhibited peaks at 855.5 and 873.2 eV, respectively. Those binding energy values were higher than NiCo₂S₄ and lower than NiFe LDH NWs, proving the electronic interactions between NiFe LDH and NiCo₂S₄ (Figure 5i). The peaks at 724.5 and 712.5 eV originated from Fe 2p_{1/2} and Fe 2p_{3/2} of Fe³⁺ in the Fe 2p of NiCo₂S₄@NiFe LDH (Figure 5j). The positive shifts of the binding energies of Fe 2p_{1/2} and Fe 2p_{3/2} suggests the electron-donating ability of Fe in NiCo₂S₄@NiFe LDH. These observations indicate strong electronic interactions of NiCo₂S₄/NiFe LDH heterointerfaces. These strong electronic interactions affect the charge distribution between NiCo₂S₄ and NiFe LDH, improving charge transport and enhancing electrocatalytic performance. NiCo₂S₄@NiFe LDH exhibited an E_{1/2} of 0.85 V for ORR and an excellent operating potential E_{j=10} of 0.287 V, with a Tafel slope of 86.4 mV dec⁻¹ for OER in 0.1 M KOH (Figure 5k).

Although other LDHs, such as NiMn, CoMn, and CoNi, have also been reported as effective OER catalysts due to their excellent activity and stability, such studies are in the early stages of development of a bifunctional catalyst for rechargeable ZABs [99–102]. Unlike the well-known NiFe LDH, which has been modified or coupled with other ORR catalysts by various strategies in an effort to make an effective bifunctional catalyst, other LDH-based catalysts have mostly been developed by anchoring them with highly porous and conductive substrates, such as nitrogen-doped graphene or carbon. Pure NiMn LDH and NiCo₂O₄@NiMn LDH core-shell arrays on Ni foam coated on carbon paper and carbon cloth exhibited promising OER performance [99,100]. Although the simple coating method could not protect such conventional OER catalysts from corrosion, excellent OER activity of NiMn LDH and NiCo₂O₄@NiMn was achieved due to their large surface area and unique porous structure which enable charging at low potential, resulting in a decreased corrosion rate of the carbon-based cathode and enhanced stability.

Recently, porous N, P dual-doped graphene aerogel (NPGA) was used as a 3D framework for anchoring CoMn LDH nanosheets, owing to its excellent ORR activity and electrical conductivity, making it an excellent bifunctional catalyst [103]. CoMn LDH nanosheets were uniformly distributed without aggregation on both sides of NPGA, which had a high active surface area, resulting in synergistically enhanced bifunctional activity and stability of CoMn-LDH/NPGA compared to either CoMn-LDH/GA composite or CoMn LDH, GA, and NPGA components. The resulting CoMn-LDH/NPGA showed an E_{1/2} of 0.868 V for ORR and an excellent operating potential E_{j=10} of 0.31 V, with a Tafel slope of 64.1 mV dec⁻¹ for OER in 0.1 M KOH.

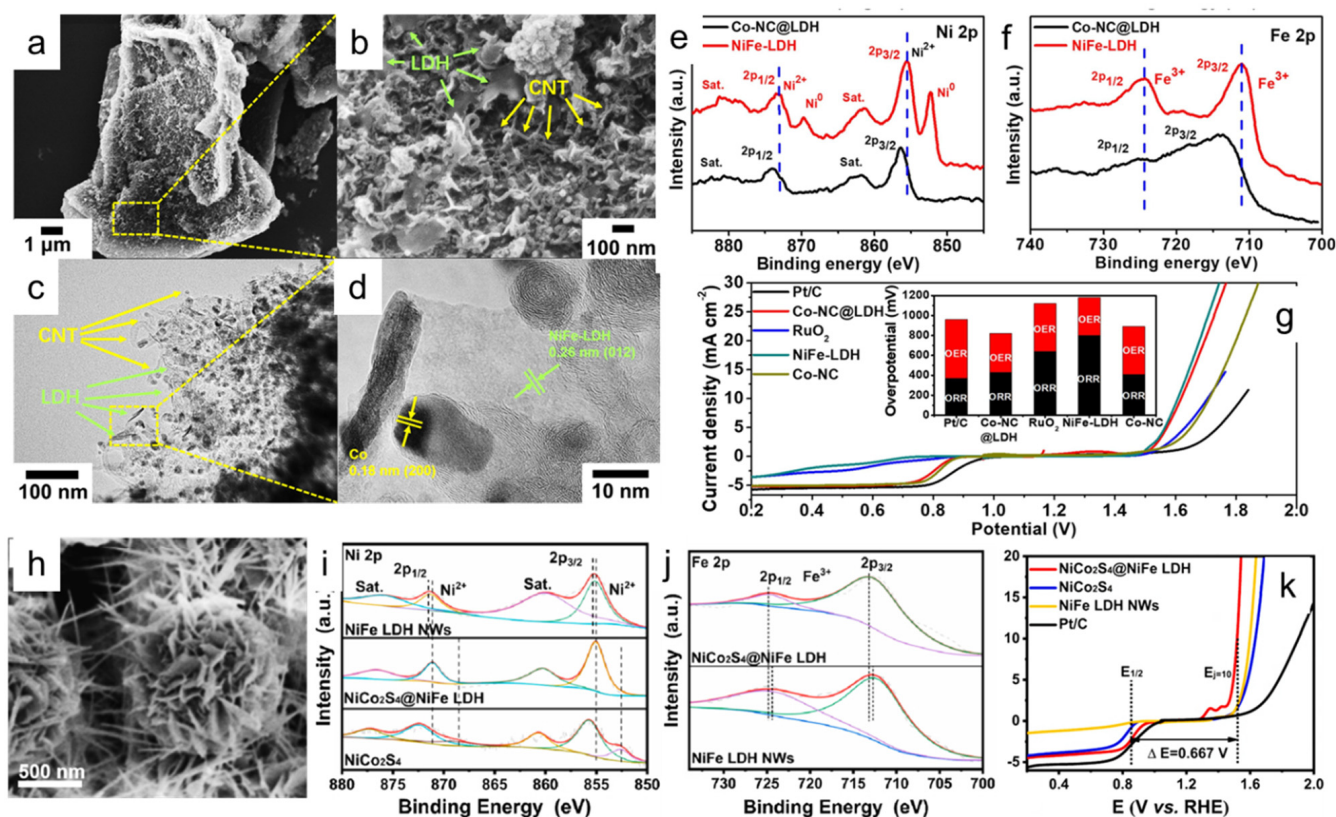


Figure 5. Structural characterization and electrochemical performance of Co-NC@LDH and NiCo₂S₄@NiFe LDH. (a,b) Co-NC@LDH at different magnifications; (c,d) TEM and HRTEM images of Co-NC@LDH. (e,f) Ni 2p and Fe 2p XPS spectra of NiFe-LDH and Co-NC@LDH. (g) LSV curves of Pt/C, Co-NC@LDH, RuO₂, NiFe-LDH, and Co-NC for OER and ORR in O₂-saturated 0.1 M KOH at 1600 rpm; inset shows potential differences between E_{1/2} of ORR and E_{j=10} of OER for different catalysts. Reproduced from [95], copyright 2020, Elsevier. (h) SEM image of NiCo₂S₄@NiFe LDH. (i) XPS spectra of Ni 2p in NiCo₂S₄@NiFe LDH, NiCo₂S₄, and NiFe LDH nanowires. (j) XPS spectra of Fe 2p in NiCo₂S₄@NiFe LDH and NiFe LDH nanowire. (k) LSV curves of NiCo₂S₄@NiFe LDH, NiCo₂S₄, and NiFe LDH nanowires and Pt/C with a scan rate of 5 mV s⁻¹ at 1600 rpm. Reproduced from [98], copyright 2020, Elsevier.

The oxygen evolution reaction (OER) plays a vital role in energy conversion and storage systems, such as CO₂ conversion, hydrogen production, and rechargeable metal-air batteries. However, OER requires four proton-coupled electron transfers to form an oxygen-oxygen double bond, making it thermodynamically and kinetically unfavourable. Thus, an electrocatalyst should be introduced to reduce the overpotential of OER and enhance the reaction rate. IrO₂ and RuO₂ have been considered the most active commercial OER catalysts, but the instability caused by their oxidation in alkaline electrolytes under high anodic potential, their scarcity, and their attractiveness limit their practical application. In this context, layered double hydroxides (LDHs) have risen as one of the most effective OER catalysts due to their excellent activity and stability in OER in alkaline conditions, structural and compositional flexibility, ease of synthesis, and low cost.

6. Metal Chalcogenides as Advanced Bifunctional Catalysts in Zn-Air Batteries

Many bifunctional electrocatalysts, such as carbon-based composites, transitional metal oxides, chalcogenides, and layered double hydroxides, have been developed to combine ORR and OER functions in an electrode. Among them, nitrogen-doped carbon-based materials are significant components of OER. Metal dichalcogenides, especially transitional metal sulphides, have received significant interest because of their excellent conductivity

and activity [104]. N and S co-doped graphene nanosheets (GNs) integrated with CoS_x nanoparticles were an effective bifunctional catalyst with good cycling stability in rechargeable ZABs [105]. In another study, $\text{CoS}_x@\text{PCN}/\text{rGO}$ (PCN, porous carbon nitride), which was synthesized by sulfurization of Co-containing PCN/rGO, showed excellent activity and stability in both oxygen evolution and reduction reactions [106]. The enhanced catalytic performance of $\text{CoS}_x@\text{PCN}/\text{rGO}$ originates from the porous morphology and sufficiently exposed active sites for oxygen-related reactions. The low Tafel slope of 44 mV dec^{-1} with $E_{j=10}$ of 0.34 V proves the ultimate contact among catalyst components and ease of mass transport at the interface between catalyst and electrolyte. Similarly, N and S co-doped CNTs decorated with porous graphene layer-encapsulated Co_9S_8 nanoparticles, and ZIF-derived $\text{Co}_9\text{S}_8/\text{C}$ coated with conductive graphene nanosheets, acted as catalysts for oxygen-related reactions in which the Co_9S_8 nanoparticles were responsible for the OER [107,108].

Replacing a part of the Co atoms in CoS_x also improved the catalytic activity in the OER. Bifunctional catalysts composed of rGO-wrapped $\text{Co}_{9-x}\text{Fe}_x\text{S}_8/\text{Co,Fe-N-C}$ (Co, Fe, N co-doped carbon) hybrids ($\text{S-Co}_{9-x}\text{Fe}_x\text{S}_8@\text{rGO}$) demonstrated that CoFeS was OER active and Co, Fe-N-C was ORR active [109]. A surprisingly low $E_{j=10}$ of 0.29 V was achieved with this catalyst, while a high $E_{1/2}$ of 0.84 V was maintained. Jiang et al. reported the activity of $(\text{Fe, Co, Ni})_9\text{S}_8$ nanoparticles embedded in a N and S co-doped interconnected carbon nanofiber network in ORR and OER [110]. In another attempt, nanoparticles of Co_8FeS_8 supported on N, S-doped carbon microparticles were prepared by heat treatment of silica-protected Fe and Co-modified S-containing polyphthalocyanine in Ar atmosphere at different temperatures ($(\text{Fe, Co})\text{SPPc-900-sp}$; 900 was the pyrolysis temperature); these were used as a bifunctional catalyst in rechargeable ZABs [111]. A moderate $E_{j=10}$ of 0.353 V and low Tafel slope of 53 mV dec^{-1} were achieved with this catalyst, while a high $E_{1/2}$ of 0.84 V was preserved. Synergistic interaction between the OER active FeCoMoS nanoflower core and nitrogen-doped graphene (NG) shell in the $\text{FeCoMoS}@\text{NG}$ was reported by Ramakrishnan et al. [112]. $\text{FeCoMoS}@\text{NG}$ nanohybrid was constructed from a flower-like FeCoMoS nanostructure and NG framework, as shown in Figure 6a. The chemical state of Fe, Co, and Mo in pristine FeCoMoS and $\text{FeCoMoS}@\text{NG}$ was recorded by XPS analysis, and is presented in Figure 6b–d. Peaks for Fe 2p, Co 2p, and Mo 3d spectra had lower intensity than FeCoMoS nanostructures, proving the formation of the core shell in the $\text{FeCoMoS}@\text{NG}$ nanohybrid. Such core-shell structure enhanced the electron-transport kinetics and durability of the active FeCoMoS nanoflowers. The best performance of the $\text{FeCoMoS}@\text{NG}$ catalyst was a low $E_{j=10}$ of 0.238 V in OER, a superior ORR $E_{1/2}$ of 0.83 V , and exceptional durability. The high specific surface area, porous networks, active catalytic sites, and interaction between the FeCoMoS nanoflower core and NG shell caused the superb activity of the $\text{FeCoMoS}@\text{NG}$ catalyst.

Ni_xSe ($0.5 \leq x \leq 1$) nanocrystals were moderate electrocatalysts for the ORR, OER, and HER in alkaline conditions [113]. The catalytic activity depended on the crystal structure and composition. $\text{Ni}_{0.75}\text{Se}$ exhibited the best ORR performance among the investigated compositions, while $\text{Ni}_{0.5}\text{Se}$ outperformed the others in OER and HER activity. The high activity of $\text{Ni}_{0.75}\text{Se}$ and $\text{Ni}_{0.5}\text{Se}$ originated from the pyrite-type crystal structure and Se enrichment, which was the active centre for the H_2O -related reaction [114]. Overpotential ($E_{j=10}$) of 0.33 and 0.36 V was observed on electrodes using $\text{Ni}_{0.5}\text{Se}$ and $\text{Ni}_{0.75}\text{Se}$, respectively. The Tafel slope values were 51 and 86 mV dec^{-1} during the OER for electrodes using $\text{Ni}_{0.5}\text{Se}$ and $\text{Ni}_{0.75}\text{Se}$, respectively. The $\text{Ni}_{0.75}\text{Se}$ nanocrystal exhibited moderate ORR activity with an E_{onset} and $E_{1/2}$ of 0.83 and 0.74 V , respectively. Zheng et al. also reported that hollow structure $\text{Ni}_x\text{Co}_{0.85-x}\text{Se}$ nanospheres exhibited better OER and ORR activity than either $\text{Co}_{0.85}\text{Se}$ or $\text{Ni}_{0.85}\text{Se}$ [115]. An $E_{j=10}$ of 0.305 V and $E_{1/2}$ of 0.78 V were achieved with this catalyst. From those results, it seemed that the aliovalent substitution of a part of Ni by Co could improve the oxygen-related catalytic activity of Ni_xSe .

Cao et al. prepared $\text{NiS}_2/\text{CoS}_2$ nanohybrids with heterostructural interfaces and used them as a bifunctional catalyst for a rechargeable ZAB [116]. The combination of

lattice distortion, electronic modulation, and synergistic effect between NiS₂ and CoS₂ domains gave the NiS₂/CoS₂ nanocrystal effective catalytic properties. The NiS₂/CoS₂ nanohybrids displayed an E_{j=10} of 0.295 V, a low Tafel slope value of 51 mV dec⁻¹, an ORR onset potential of 0.90 V, and an E_{1/2} of 0.79V. Yin et al. reported that oxygen vacancies at the interface of cobalt–nickel sulphide porous nanowires (NiS₂/CoS₂-O NWs) exhibited excellent electrochemical catalytic activity [117]. Figure 6e shows the pores and rough surface of NiS₂/CoS₂-O NWs, originating from the sulphur loss and oxide reorganization on the surface during the preparation process. HRTEM of NiS₂/CoS₂-O NWs revealed lattice fringe spacing of cubic NiS₂, CoS₂, CoO_x, and NiO (Figure 6f). The element mapping of NiS₂/CoS₂-O NWs (Figure 6g) presented uniform Ni, Co, O, and S distribution across the nanowire with a reduced sulphur signal. XPS spectra of the S 2p of NiS₂/CoS₂ NWs and NiS₂/CoS₂-O NWs also indicated that the sulphide on the surface disappeared after in situ electrochemical reaction (Figure 6h). The O 1s spectra (Figure 6i) further confirmed the oxide products on the surface of NiS₂/CoS₂-O NWs. The O 1s spectrum of NiS₂/CoS₂-O NWs was composed of three categories (denoted as O1, O2, and O3), assigned to the metal–O band, oxygen vacancies, and hydroxy species of adsorbed water molecules. The large area of O₂ suggests abundant oxygen vacancies created during the oxidation of NiS₂/CoS₂ NWs. The O 1s spectrum of NiS₂/CoS₂ NWs suggested that the O present was in the adsorbed water.

The density functional theory (DFT) calculations revealed that the interfaces of (100)Co(Ni)S₂|| (104)Co(Ni)O, (010)Co(Ni)S₂|| (010)Co(Ni)O were the most matched interfaces, with a strain of only 5%, in NiS₂/CoS₂-O NWs. Calculation results for the energetic profiles of OER showed intermediate states and energetic profiles for CoS₂-O, NiS₂-O, and NiS₂/CoS₂-O, of which NiS₂/CoS₂-O required a lower overpotential (0.47 V) than CoS₂-O (0.61 V) and NiS₂-O (0.64 V). The theoretical prediction agreed with the experimental results, which show that an exceptionally low E_{j=10} of 0.235 V and a Tafel slope value of 31 mV dec⁻¹ were obtained with the electrode using this catalyst. In a different study, Guo et al. employed N, P-doped CoS₂ nanoclusters embedded inside TiO₂ nanoporous film (NPF) (denoted as N, P/CoS₂@TiO₂) as a catalyst in an air electrode in a rechargeable ZAB [118]. The morphology of TiO₂ NPFs was ordered honeycomb with a pore size of about 50 nm and a thickness of less than 70 nm (Figure 6j). After the preparation process, the obtained N, P/CoS₂@TiO₂ resembled the morphology of pristine TiO₂ NPFs (Figure 6k), in which all TiO₂ holes and walls were covered by highly ordered CoS₂ nanoclusters (Figure 6l). CoS₂ also filled inside the TiO₂ pores, as shown by cross-section TEM (Figure 6m). HRTEM showed the (100) planes of pyrite CoS₂ with lattice fringes of 0.54 nm (Figure 6n). The lattice spacings of the (111), (211), and (100) planes were identified to be 0.32, 0.23, and 0.54 nm, respectively. This proved that N- and P-doping significantly improved catalytic activity and stability, while the nanoporous TiO₂ structure prevented the catalyst particles from aggregating. In particular, N-doping enhanced the conductivity and electrochemical activity of the NPFs, while P-doping endowed the electrode with a passivated surface and improved stability. Thus, excellent OER performance was obtained, with an E_{j=10} of 0.26 V (Figure 6o).

The transitional metal chalcogenides exhibit high activity in oxygen evolution reaction, and this ability could be boosted by the aliovalent substitution of metal ion or oxygen doping. The formation of an interface between two types of chalcogenides increases their ORR activity and thus makes them bifunctional catalysts. However, the composite with nitrogen-doped carbonaceous materials outperforms in ORR activity, making it an excellent bifunctional catalyst, because N-doped carbonaceous materials are natively ORR catalysts.

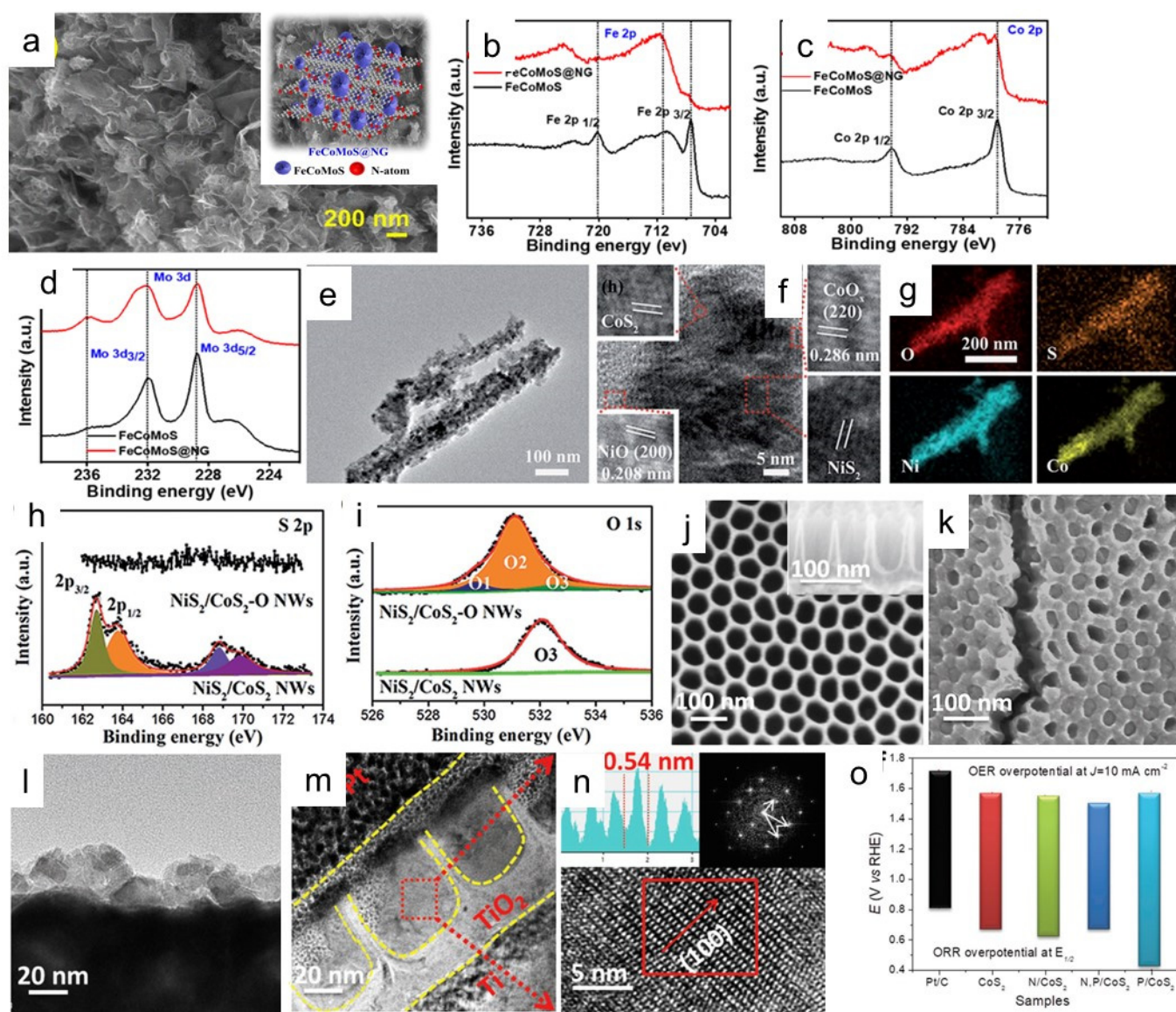


Figure 6. Structural characterization and electrochemical performance of typical chalcogenides. (a) SEM image of FeCoMoS@NG nanohybrid. (b–d) Comparative XPS spectra of (b) Fe 2p, (c) Co 2p, and (d) Mo 3d of FeCoMoS and FeCoMoS@NG. Reproduced from [112], copyright 2020, Elsevier. (e–g) TEM and HRTEM images and element mapping of NiS₂/CoS₂-O NWs. (h,i) XPS spectra of S 2p and O 1s of NiS₂/CoS₂ NWs and NiS₂/CoS₂-O NWs. Reproduced from [117], copyright 2017, Wiley-VCH Verlag GmbH & Co. (j,k) SEM images of pristine TiO₂ nanoporous film (inset shows cross-sectional SEM view) and N, P/CoS₂@TiO₂, respectively. (l,m) TEM images and (n) HRTEM images of N, P/CoS₂@TiO₂ with lattice spacing and fast Fourier transform (FFT) patterns inserted. (o) ORR and OER overpotentials of samples ($\Delta E = E_{j=10} - E_{1/2}$). Reproduced from [118], copyright 2018, Wiley-VCH Verlag GmbH & Co.

7. Metal Oxides as Advanced Bifunctional Catalysts in Zn–Air Batteries

An effective bifunctional catalyst is needed to address the slow kinetics of OER and ORR. Metal oxides have attracted much interest due to their excellent catalytic activity and abundance. The metal oxides themselves can act as either ORR or OER catalysts, but they have low intrinsic electronic conductivity, so several ways to integrate them with carbonaceous materials have been developed to fabricate bifunctional catalysts [119–123]. Several metal oxides were coupled with N-doped carbonaceous materials for ZABs. Manganese oxides have also attracted interest because of their low cost and high efficiency [120,121].

Sumboja et al. prepared MnO_x directly on carbon paper and used it as an air electrode for ZAB [122]; the manganese oxide was grown directly on carbon paper through a simple immersion process. XPS results revealed the presence of a mixture of MnII, MnIII, and MnIV phases with peaks at 652.5 eV ($2p_{1/2}$) and 640.2, 641.1, 642.9 eV ($2p_{3/2}$), respectively. The even distribution of MnO_x within the pore system of the carbon paper promoted oxygen-related reactions. Solution resistance (R_s), resistance at the electrode/electrolyte interface (R_{int}), and resistance of charge transfer during the electrochemical process (R_{ct}) of the rechargeable ZAB using the mentioned electrode were much smaller than those of the electrode using MnO_x powder dispersed on carbon paper. MnO_2 nanosheets were modified with Co, Ni, or Fe to improve the ORR ability for bifunctional oxygen catalysts [124]. Improvements in ORR and OER were observed in Co- MnO_2 , because the modification created additional active sites for OER and induced more oxygen defects to further facilitate ORR.

Besides manganese oxides with a tuneable oxidation state, Co_3O_4 and its composites have also been investigated as potential bifunctional catalysts for ZABs [125–127]. The hierarchical structure—hollow Co_3O_4 nanospheres embedded in nitrogen-doped carbon nanowall arrays on flexible carbon cloth (NC- Co_3O_4 /CC)—was derived from a metal-organic framework precursor by calcination processes. The nanograin structure of Co_3O_4 particles exhibited promising catalytic performance, with an $E_{1/2}$ of 0.87 V and an $E_{j=10}$ of 0.358 V. A 1D/2D hybrid $\text{Co}_{1-x}\text{Fe}_x\text{O@NC}$ (N- and C-doped $\text{Co}_{1-x}\text{Fe}_x\text{O}$) nanostructure grown on flexible carbon cloth ($\text{Co}_{1-x}\text{Fe}_x\text{O@NC/CC}$) exhibited good OER and ORR kinetics [128]. The 2D nanosheets on the 1D nanowire frame of $\text{Co}_{1-x}\text{Fe}_x\text{O@NC}$ are illustrated in Figure 7a,b. The Co $2p_{3/2}$ binding energy of $\text{Co}_{0.32}\text{Fe}_{0.68}\text{O@NC}$, $\text{Co}_{0.51}\text{Fe}_{0.49}\text{O@NC}$, and $\text{Co}_{0.33}\text{Fe}_{0.67}\text{O@NC}$ shifted about 0.17, 0.43, and 0.64 eV compared to CoO@NC (Figure 7c). The Co 2p peak shifting with increased Fe loading proved the electron transfer from Fe to Co.

The N 1s spectra are composed of three components: graphitic-N (401.4 eV), metal-bonded N (399.4 eV), and NO_3^- (406.7 eV) (Figure 7d). The increased metal-bonded N of $\text{Co}_{0.68}\text{Fe}_{0.32}\text{O@NC/CC}$ enhanced the OER and ORR performance, because metal-bonded N has been identified as an active site for OER and ORR. In fact, the voltage gap of $\text{Co}_{0.68}\text{Fe}_{0.32}\text{O@NC/CC}$ ($\Delta E = E_{j=10} - E_{1/2}$) was 0.68 V, which was less than that of CoO@NC/CC , $\text{Co}_{0.51}\text{Fe}_{0.49}\text{O@NC/CC}$, $\text{Co}_{0.33}\text{Fe}_{0.67}\text{O@NC/CC}$, $\text{Co}_{0.33}\text{Fe}_{0.67}\text{O/CC}$, or Pt/C- IrO_2 (Figure 7e). In another attempt, CoO_x clusters supported on a nitrogen-doped mesoporous carbon (CoO_x/NMC) composite showed enhanced bifunctional electrocatalytic performance in alkaline media compared with Pt/C and Ir/C catalysts [129]. Owing to their precursor CoOOH species anchored on NMC, well-dispersed CoO_x clusters with a size of 2–3 nm were formed and exhibited good catalytic performance. The high-resolution Co 2p XPS spectra illustrated the presence of mixed cobalt valence states of $\text{Co}^{2+}/\text{Co}^{3+}$ of CoO and Co_3O_4 in CoO_x/NMC , with two non-satellite peaks at 780.7 and 796.5 eV, respectively. In addition, pyridinic-N and graphitic-N (centred at binding energies of 400.8 and 398.5 eV, respectively) could enhance interactions between NMC and CoO_x clusters. The fine structure of the composite components and ultimate contact among them resulted in excellent catalytic performance, with an $E_{1/2}$ of 0.907 V and an $E_{j=10}$ of 0.269 V.

Wang et al. reported the fabrication and catalytic properties of vertically aligned porous nanoarrays composed of ultrafine nitrogen-doped cobalt oxide (NP- Co_3O_4) nanoparticles (4–5 nm) on carbon cloth (CC), through calcination of Co-based zeolitic-imidazolate framework (Co-ZIF) nanoarrays (Figure 7f) [130]. The low-temperature process allowed the Co nodes of Co-ZIF to oxidize into ultrafine Co_3O_4 nanoparticles. The lattice distances of 2.02, 2.44, 2.87, and 4.67 Å (Figure 7g) indexed to (400), (311), (220), and (111) oriented facets of Co_3O_4 . Co–N bonds in the NP- $\text{Co}_3\text{O}_4/\text{CC}$ were detected using XPS, with Co $2p_{3/2}$ and Co $2p_{1/2}$ peaks appearing at 781.5 and 796.5 eV, respectively. In addition, the existence of N^{3-} with a peak at 398.7 eV (Figure 7h) confirmed the Co–N bonds. Nitrogen doping could generate high oxygen vacancies on the surface of NP- Co_3O_4 , improving its electronic conductivity and catalytic properties. Three other types of oxygen species were found in NP- $\text{Co}_3\text{O}_4/\text{CC}$: O_L (529.7 eV, lattice oxygen in the Co_3O_4 phase), O_D (531.0 eV, oxygen-

deficient Co_3O_4), and O_C (531.9 eV, chemisorbed and dissociated oxygen species (O_2^- , O_2^- , or O^-) and OH^-) (Figure 7i). The ORR and OER current density of NP- $\text{Co}_3\text{O}_4/\text{CC}$ was superior compared to that generated by Pt/C and Ir/C catalysts. Wang et al. also prepared and investigated the structure and catalytic activity of carbon nanotube (CNT)-grafted and nano Co_3O_4 -doped porous carbon [131]. Co- N_x bonds in the Co_3O_4 -doped porous carbon were detected using XPS, with Co 2p_{3/2} and Co 2p_{1/2} peaks at 778.4 eV and 793.5 eV, respectively. The peak position of Co- N_x in Co_3O_4 -doped porous carbon was very different from the peaks of CoO_x/NMC and NP- Co_3O_4 . The Co 2p_{3/2} and Co 2p_{1/2} peaks in CoO_x/NMC and NP- Co_3O_4 agreed with each other. Although the reason was unclear, the presence of Co metal in Co_3O_4 -doped porous carbon altered the chemical environment around Co- N_x bonding, hence the binding energy was changed.

Composites of spinel and perovskite metal oxides could also serve as bifunctional catalysts for oxygen-related reactions [132–134]. Kosasang et al. investigated the electrocatalytic activity of bimetallic oxides such as CoMn_2O_4 and NiMn_2O_4 and trimetallic spinel-type $\text{Co}_{0.5}\text{Ni}_{0.5}\text{Mn}_2\text{O}_4$ [135]. In situ X-ray absorption spectroscopy (XAS) showed that Co had the primary role in the ORR process, while the three metals made the same contribution to OER activity. The oxidation state of Mn, Co, and Ni during the reactions, equivalent to 0.08, 0.26, and 0.15 for ORR and 0.13, 0.12, and 0.14 for OER, respectively, suggested that they underwent oxidation and reduction. Therefore, the superior performance of $\text{Co}_{0.5}\text{Ni}_{0.5}\text{Mn}_2\text{O}_4$ catalyst was due to the active Co for the OER active site and the Co, Mn, and Ni for the ORR active sites. It was also found that Mn_3O_4 -based spinel oxides were active for ORR, and that Co-doping further extended the activity while Fe dopant reduced it [136]. For OER, Cr, V, or Ni dopants could significantly enhance the activity of FeCo-based oxides; among them, Cr was the most effective. The performance of the $(\text{FeCoNi})_3\text{O}_4/\text{Mn}_3\text{O}_4$ nanocomposite was comparable to that of the commercial Pt/C + IrO_2 catalyst. Besides transitional metals, sulphur (S) doping in oxide perovskites (such as LaCoO_3 , LaNiO_3 , and LaFeO_3) could also accelerate oxygen electrocatalytic activity, because those reactions in oxide perovskites are strongly dependent on electronic conductivity and electron configurations [137]. The La 3d XPS spectra indicated that La existed in the La^{3+} form in both LaCoO_3 and S5.84%– LaCoO_3 , with the presence of two peaks of La 3d_{3/2} (850.4 and 854.7 eV) and 3d_{5/2} (833.5, 837.5 eV). A slight shift (0.3 eV) towards lower binding energy in the Co 2p spectrum of S5.84%– LaCoO_3 implied that the Co oxidation state became lower due to the S doping. In addition, S doping also introduced more oxygen defects, thus enhancing the interaction of hybrids and the absorbed oxygen-containing species. As a result of structural change, the catalytic activity of S5.84%– LaCoO_3 was better than that of bare LaCoO_3 .

The introduction of S into cobalt manganese spinel oxides (CoMn_2O_4) also boosted its bifunctional catalytic activity [138]. It was shown that an appropriate amount of S could be introduced into CoMn_2O_4 without any impurity phase (Figure 7l–n). XPS revealed that S-doping enhanced the concentrations of active Mn^{4+} , Co^{3+} , and oxygen defects, while the DFT results suggested that the metal–oxygen bonds of S– CoMn_2O_4 could facilitate the energy gap of Co 3d O 2p and Mn 3d O 2p centres and thus enhance OER/ORR activity. Indeed, the relative intensity of $\text{Co}^{3+}/\text{Co}^{2+}$ for S– CoMn_2O_4 (0.81) was higher than CoMn_2O_4 (0.67), and the spin state of Co^{3+} could promote transformation from a low to an intermediate spin state, thus accelerating the electron transfer of the ORR and OER processes. Lattice oxygen (O1, 529.7 eV), oxygen defect sites (O2, 531.3 eV), and surface-attached oxygen (O3, 532.6 eV) existed in CoMn_2O_4 . In addition, oxygen defects appeared with a higher ratio of O2/O1 (5.42) by S-doping in CoMn_2O_4 (Figure 7o). The S 2p_{3/2} and S 2p_{1/2} peaks at 160.7 and 163.2 eV indicated the existence of S^{2-} in doped CoMn_2O_4 due to the replacement of O by S (Figure 7p). The oxygen vacancies significantly improved the electronic conductivity of S– CoMn_2O_4 compared to CoMn_2O_4 (Figure 7q). As is widely accepted, high electrical conductivity favours the electron transfer process of electrocatalysis; therefore, S– CoMn_2O_4 showed better performance, with an $E_{1/2}$ of 0.87 V and an $E_{j=10}$ of 0.358 V, than CoMn_2O_4 , with an $E_{1/2}$ of 0.72 V and an $E_{j=10}$ of 0.410 V.

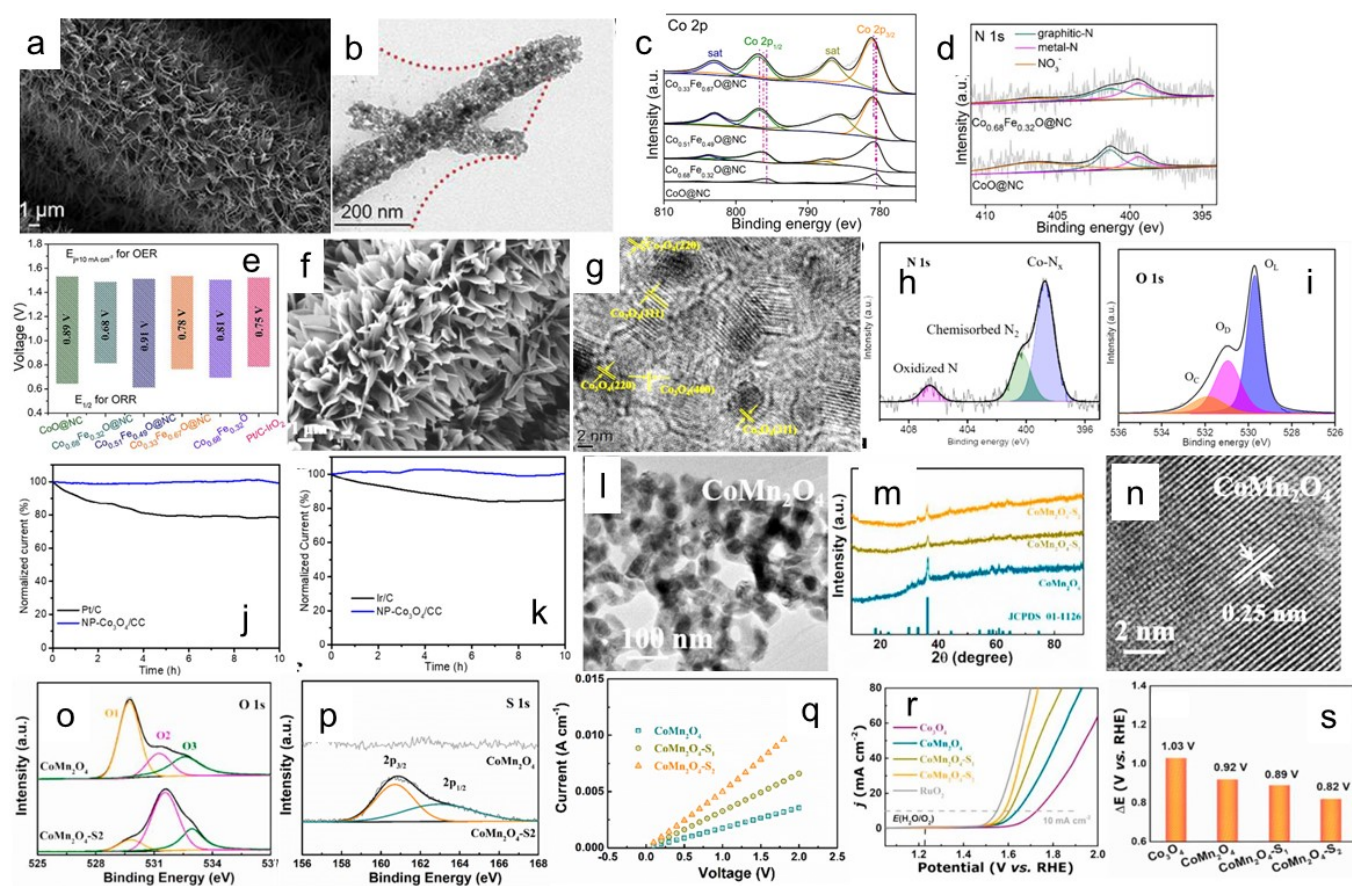


Figure 7. Characterization and electrochemical performance of typical oxide-based catalysts. (a,b) SEM and TEM images of $\text{Co}_{0.68}\text{Fe}_{0.32}\text{O@NC}$. (c,d) High-resolution XPS spectra of Co 2p and N 1s of $\text{Co}_{0.68}\text{Fe}_{0.32}\text{O@NC}$. (e) Bar plots of voltage gap between $E_{j=10}$ and $E_{1/2}$. Reproduced from [128], copyright 2020, Elsevier. (f,g) SEM and HRTEM images of NP- $\text{Co}_3\text{O}_4/\text{CC}$. (h,i) High-resolution XPS spectra of N 1s and O 1s of NP- $\text{Co}_3\text{O}_4/\text{CC}$. (j) ORR stability evaluation of NP- $\text{Co}_3\text{O}_4/\text{CC}$ and Pt/C at a constant potential of 0.7 V. (k) OER stability evaluation of NP- $\text{Co}_3\text{O}_4/\text{CC}$ and Ir/C at a constant potential of 1.56 V. Reproduced from [130], copyright 2020, Elsevier. (l) TEM images of CoMn_2O_4 . (m) XRD patterns of CoMn_2O_4 , $\text{CoMn}_2\text{O}_4\text{-S1}$, and $\text{CoMn}_2\text{O}_4\text{-S2}$. (n) Lattice fringe image of CoMn_2O_4 . (o,p) High-resolution XPS spectra of O 1s and S 1s in CoMn_2O_4 and $\text{CoMn}_2\text{O}_4\text{-S2}$. (q) Electronic conductivity of CoMn_2O_4 , $\text{CoMn}_2\text{O}_4\text{-S1}$, and $\text{CoMn}_2\text{O}_4\text{-S2}$ measured by two probe method. (r) OER LSV curves for Ir/C, Co_3O_4 , CoMn_2O_4 , $\text{CoMn}_2\text{O}_4\text{-S1}$, and $\text{CoMn}_2\text{O}_4\text{-S2}$. (s) ΔE of OER and ORR for Ir/C, Co_3O_4 , CoMn_2O_4 , $\text{CoMn}_2\text{O}_4\text{-S1}$, and $\text{CoMn}_2\text{O}_4\text{-S2}$. Reproduced from [138], copyright 2021, Elsevier.

Transitional metal oxides are abundant, stable, and cost-effective, but their performance as bifunctional catalysts is still unsatisfactory based on the requirements of commercialized ZABs. Numerous research articles have reported discoveries on metal oxide-based bifunctional catalysts, and most of them focused on modifying conventional catalysts. S- and Co-doping seem to be the most effective way to improve their performance. In addition, excellent contact among electrode composites, catalysts, and carbonaceous materials is a critical element in obtaining excellent air electrodes for ZABs.

Tables 2 and 3 summarize the OER ($E_{1/2}$) and ORR ($E_{j=10}$) of several catalysts. The $E_{1/2}$ of catalysts belonging to noble metals, N-doped carbonaceous materials, layered double hydroxides, metal chalcogenides, and metal oxide catalysts varied from 0.7 to 0.9 V vs. RHE. Catalysts based on metallic nanoparticles exhibited similar results, ranging from 0.8 to 0.9 V vs. RHE. The $E_{j=10}$ of N-doped carbonaceous materials was generally higher than that of the others. Catalysts based on metallic nanoparticles, metal chalcogenides, and layered double hydroxides showed promising activity in the OER. Thus, an excellent

bifunctional catalyst should be a composite of N-doped carbonaceous materials and either metallic nanoparticles, metal chalcogenides, or layered double hydroxides.

Table 2. ORR performance of catalysts based on noble metals, N-doped carbonaceous materials, metallic nanoparticles, metal chalcogenides, layered double hydroxides, and metal oxides.

Number	Catalyst	$E_{1/2}/V$	Electrolyte	Catalyst Loadings (mg cm ⁻²)	Ref
Noble metal					
1	Fe ₃ Pt/C	0.91	0.1 M KOH	0.12	[15]
2	Fe ₃ Pt/Ni ₃ FeN	0.93	0.1 M KOH	0.12	[15]
3	Co(OH) ₂ /CoPt/N-CN	0.83	0.1 M KOH	0.102	[17]
4	SA-PtCoF	0.88	1 M KOH	0.42	[18]
5	Pt/CoFe ₂ O ₄	0.72	0.1 M KOH	0.283	[19]
6	PtFeNC	0.895	0.1 M KOH	0.255	[16]
8	Ag/LMO-NR/RGO	0.691	0.1 M KOH	0.317	[22]
9	Ag-Cu/Ni	0.691	0.1 M KOH	0.8	[23]
N-doped carbonaceous (NC) materials					
10	NDG _s -800	0.85	0.1 M KOH	0.204	[34]
11	SilkNC/KB	0.764	0.1 M KOH	0.6	[35]
12	GNCNTs-4	0.85	0.1 M KOH	0.51	[37]
13	NPC@CNF-950	0.88	0.1 M KOH	0.1	[36]
14	Honeycomb-600	0.837	0.1 M KOH	0.3	[38]
15	3D Fe/N-G	0.852	0.1 M KOH	0.276	[43]
16	Fe-MNC	0.85	0.1 M KOH	0.286	[44]
17	2D Fe-NG	0.86	0.1 M KOH	0.236	[45]
18	GSC-900	0.8	0.1 M KOH	0.255	[49]
19	hSNCNC	0.792	0.1 M KOH	0.127	[52]
20	DDPCN	0.87	0.1 M KOH	0.4	[53]
Metallic nanoparticle					
21	Co-N-CNTs	0.90	0.1 M KOH	0.81	[60]
22	CNCF-800	0.66	0.1 M KOH	0.25	[61]
23	Co@NCNTA-700	0.861	0.1 M KOH	1	[62]
24	Co@NC-3	0.816	0.1 M KOH	0.24	[63]
25	Co/N-CNTs@rGO	0.88	0.1 M KOH		[64]
26	Co@NC-5	0.86	0.1 M KOH	0.5	[65]
27	FeCo@NC-750	0.8	0.1 M KOH	0.4	[75]
28	<i>h</i> -FeCo alloy/N-CNFs	0.87	0.1 M KOH	0.2	[76]
29	CoFe@NCNTs	0.84	0.1 M KOH	0.8	[77]
30	Fe _{1.2} Co@NC/NCNTs	0.82	0.1 M KOH	0.2	[78]
31	Ni ₃ Fe/N-C	0.81	0.1 M KOH	0.22	[80]
32	Ni ₃ Fe/NPG-1	0.83	0.1 M KOH	1	[81]
33	Fe-enriched-FeNi ₃ /NC	0.78	0.1 M KOH	0.8	[82]
34	Ni ₃ Fe/N-S-CNTs	0.877	1 M KOH	0.42	[85]
35	FeNi/N-CPCF-950	0.867	0.1 M KOH	0.6	[84]
36	NiFe@NCNTs (Ni _{0.36} Fe _{0.64})	0.79	1 M KOH	0.408	[83]
37	FeNi ₃ @NC	0.86	0.1 M KOH	–	[139]
Layered double hydroxide					
38	MCN-LDH-1.5	0.826	0.1 M KOH	0.4	[94]
39	Co ₃ O ₄ @NiFe-2	0.76	1 M KOH	0.4	[97]
40	NiCo ₂ S ₄ @NiFe	0.85	0.1 M KOH	–	[98]
41	NiMn (Ni ₃ Mn ₁)	0.74	0.1 M KOH	0.2	[99]
42	Hollow sphere Co ₂ Mn ₁	0.83	0.1 M KOH	0.51	[101]
43	CoNi-NS/rGO	0.85	1 M KOH	0.48	[102]
44	CoMn-LDH/NPGA	0.868	0.1 M KOH	0.255	[103]

Table 2. Cont.

Number	Catalyst	$E_{1/2}/V$	Electrolyte	Catalyst Loadings (mg cm^{-2})	Ref
Metal chalcogenides					
45	CoS _x @PCN/rGO	0.78	0.1 M KOH	0.408	[106]
46	Co/N/S-800	0.831	0.1 M KOH	0.1	[107]
47	S-Co _{9-x} Fe _x S ₈ @rGO	0.84	0.1 M KOH	0.5	[109]
48	FeCoMoS@NG	0.83	0.1 M KOH	0.21	[112]
49	(Fe,Co)SPPc-900-sp	0.83	0.1 M KOH	0.28	[111]
50	Ni _{0.75} Se	0.74	1 M KOH		[113]
51	NiS ₂ /CoS ₂	0.79	0.1 M KOH		[116]
52	NiS ₂ /CoS ₂ -O NWs	0.7	0.1 M KOH		[117]
53	N, P/CoS ₂ @TiO ₂	0.71	0.1 M KOH		[118]
Metal oxides					
54	NC-Co ₃ O ₄ -90	0.87	1 M KOH		[126]
55	CoO _x /NMC	0.907	1 M KOH		[129]
56	NP-Co ₃ O ₄ /CC	0.9	1 M KOH		[130]
57	S _{5.84%} -LaCoO ₃	0.7	1 M KOH		[137]
58	S-CoMn ₂ O ₄	0.76	1 M KOH		[138]

Table 3. OER performances of catalysts based on noble metals, N-doped carbonaceous materials, metallic nano particles, metal chalcogenides, layer doubled hydroxides, and metal oxides.

Number	Catalyst	Over-potential/V (10 mA cm^{-2})	Tafel Slope/mV dec^{-1}	Electrolyte	Catalyst Loadings (mg cm^{-2})	Ref
Noble metals						
1	Ni ₃ FeN	0.38		0.1 M KOH	0.12	[15]
2	Fe ₃ Pt/Ni ₃ FeN	0.365		0.1 M KOH	0.12	[15]
3	Co(OH) ₂ /CoPt/N-CN	0.32	73.4	1 M KOH	0.102	[17]
4	SA-PtCoF	0.308	68	1 M KOH	0.42	[18]
5	Pt/CoFe ₂ O ₄	0.28	88	1 M KOH	0.283	[19]
7	Ag/LMO-NR/RGO	0.49		0.1 M KOH	0.317	[22]
8	Ag-Cu/Ni	0.27		0.1 M KOH	0.8	[23]
9	Ru _{0.7} Sn _{0.3} O ₂	0.24		0.1 M KOH	0.1	[25]
N-doped carbonaceous (NC) materials						
10	NDG _s -800	0.45	132	1 M KOH	0.4	[34]
11	SilkNC/KB	0.73	109	0.1 M KOH	0.6	[35]
12	GNCNTs-4	0.37	61	0.1 M KOH	0.51	[37]
13	NPC@CNF-950	0.47	132	0.1 M KOH	0.1	[36]
14	Honeycomb-600	0.38	85.9	0.1 M KOH	0.3	[38]
15	3D Fe/N-G	0.393	71.5	0.1 M KOH	0.276	[43]
16	Fe-MNC	0.348	127	1 M KOH	0.286	[44]
17	2D Fe-NG	0.39	70.1	0.1 M KOH	0.236	[45]
18	hSNCNC	0.41	288	0.1 M KOH	0.127	[52]
Metallic nanoparticle						
19	Co-N-CNTs	0.46		0.1 M KOH	0.81	[60]
20	CNCF-800	0.41		0.1 M KOH	0.25	[61]
21	Co@NCNTA-700	0.28		0.1 M KOH	1	[62]
22	Co@NC-3	0.49	92	0.1 M KOH	0.24	[63]
23	Co/N-CNTs@rGO	0.381		0.1 M KOH		[64]
24	Co/Co-N-C	0.47		0.1 M KOH	0.382	[140]
25	Co@NC-5	0.390		0.1 M KOH	0.5	[65]
26	FeCo@NC-750	0.22	52	0.1 M KOH	0.4	[75]
27	<i>h</i> -FeCo alloy/N-CNFs	0.368	62.74	1 M KOH	0.2	[76]
28	CoFe@NCNTs	0.45	158	0.1 M KOH	0.8	[77]
29	Fe _{1.2} Co@NC/NCNTs	0.355	66	0.1 M KOH	0.2	[78]

Table 3. Cont.

Number	Catalyst	Over-potential/V (10 mA cm ⁻²)	Tafel Slope/mV dec ⁻¹	Electrolyte	Catalyst Loadings (mg cm ⁻²)	Ref
30	Ni ₃ Fe/N-C	0.310	58	1 M KOH	0.22	[80]
31	Ni ₃ Fe/NPG-1	0.329	82	0.1 M KOH	1	[81]
32	Fe-enriched-FeNi ₃ /NC	0.36	82	0.1 M KOH	0.8	[82]
33	Ni ₃ Fe/N-S-CNTs	0.215	44.1	1 M KOH	0.42	[85]
34	FeNi/N-CPCF-950	0.355	67	0.1 M KOH	0.6	[84]
35	NiFe@NCNTs (Ni _{0.36} Fe _{0.64})	0.33	74	1 M KOH	0.408	[83]
36	FeNi ₃ @NC	0.277	77	1 M KOH	–	[139]
Layered double hydroxide						
37	MCN-LDH-1.5	0.44	140	0.1 M KOH	0.4	[94]
38	Co ₃ O ₄ @NiFe-2	0.31	55.5	1 M KOH	0.4	[97]
39	NiCo ₂ S ₄ @NiFe	0.287	86.4	0.1 M KOH	–	[98]
40	NiMn (Ni ₃ Mn ₁)	0.38	40	1 M KOH	0.2	[99]
41	NiCo ₂ O ₄ @NiMn	0.255	62.4	1 M KOH	2.0 ± 0.2	[100]
42	Hollow sphere Co ₂ Mn ₁	0.255	57	1 M KOH	2.0	[101]
43	CoNi-NS/rGO	0.33	62	1 M KOH	0.48	[102]
44	CoMn-LDH/NPGA	0.31	64.1	0.1 M KOH	0.255	
Metal chalcogenides						
45	CoS _x @PCN/rGO	0.34	44	0.1 M KOH	0.408	[106]
46	Co/N/S-800	0.361	102	0.1 M KOH	0.1	[107]
47	S-Co _{9-x} Fe _x S ₈ @rGO	0.29	66	0.1 M KOH	0.5	[109]
48	FeCoMoS@NG	0.238	51	0.1 M KOH	0.21	[112]
49	(Fe,Co)SPPc-900-sp	0.353	53	1 M KOH	0.28	[111]
50	Ni _{0.5} Se	0.33	51	1 M KOH		[113]
51	NiS ₂ /CoS ₂	0.295	51	0.1 M KOH		[116]
52	NiS ₂ /CoS ₂ -O NWs	0.235	31	1 M KOH		[117]
53	N, P/CoS ₂ @TiO ₂	0.26	79	0.1 M KOH		[118]
Metal oxides						
54	NC-Co ₃ O ₄ -90	0.358		1 M KOH		[126]
55	CoO _x /NMC	0.269	59.8	1 M KOH		[129]
56	NP-Co ₃ O ₄ /CC	0.330		1 M KOH		[130]
57	S _{5.84%} -LaCoO ₃	0.364	126.7	1 M KOH		[137]
58	S-CoMn ₂ O ₄	0.35	88	1 M KOH		[138]

8. Zinc–Air Battery Performance

Zinc–air batteries are mainly composed of three components: a zinc electrode, an oxygen electrode, and an electrolyte. Even though bifunctional catalysts are essential for cell performance, other issues, such as contamination in the oxygen, degradation of the zinc electrode, and migration of zinc-based species from the zinc electrode to the oxygen electrode, also affect cell stability and overvoltage. Figure 8 displays the open-circuit voltage and peak power density of ZABs employing different catalysts. Zn-doped Ni₃FeN/nitrogen-doped graphene (Zn-Ni₃FeN/NG) exhibited moderate E_{1/2} (0.86 V) and E_{j=10} (0.37 V) compared to the others, but the cell employing this catalyst showed the highest open-circuit voltage (1.60 V) among the screening data, and was very close to the theoretical value (1.66 V) [141]. Co₂Fe₁ encapsulated in a N-doped carbon shell, Co₂Fe₁@NC, showed average values of E_{1/2} (0.85 V) and E_{j=10} (0.42 V); however, the cell using this catalyst achieved extremely high peak power density of about 423.7 mW cm⁻² [71]. High open-circuit voltage and peak power density were also observed in ZABs using NP-Co₃O₄/CC, Felix-PNC, and NiFe@NCNTs. Therefore, the number of catalytic active centres and interfaces among the components should play an essential role in the cell's open-circuit voltage and peak power density. Table 4 shows the data of typical ZAB performance. The data were chosen based on the values of open-circuit voltage (1.50 V), polarization (ΔE =

$E_{\text{charge}} - E_{\text{discharge}}$, $\Delta E < 1.0\text{V}$), and charge/discharge voltage (2.0/1.20 V), and the cells that satisfied one of these values are listed in Table 4. Most of the cells had a charge/discharge voltage that was far from the theoretical value of 1.66 V, indicating the high overvoltage of the process. However, a lack of cell analysis data, such as electrochemical impedance spectroscopy (EIS), made it difficult to determine the cause of high overvoltage. It seemed that oxygen-related reactions generated most of the overvoltage.

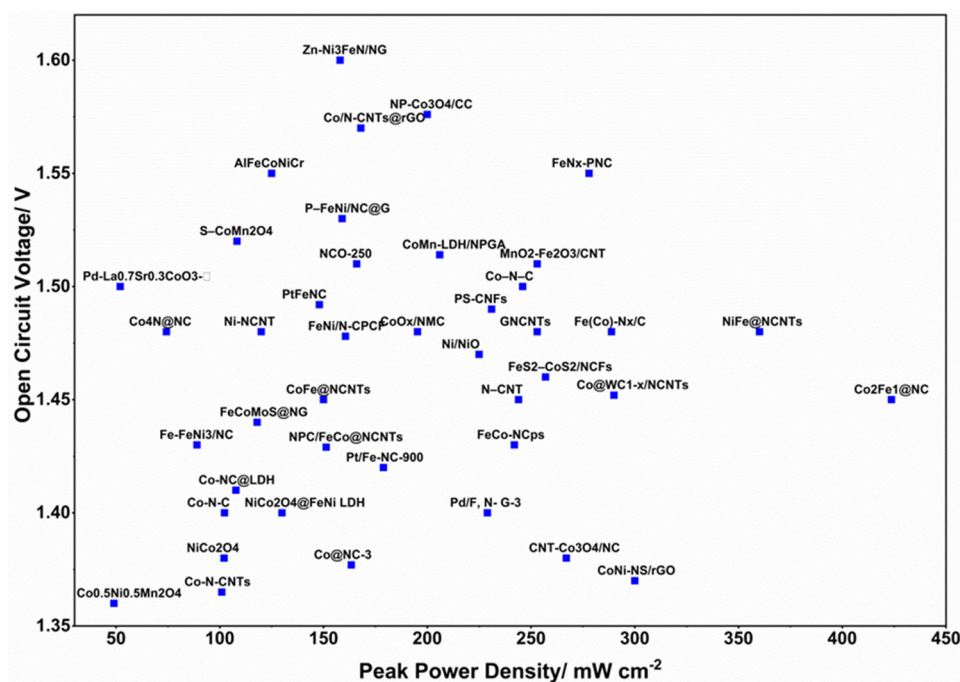


Figure 8. Open-circuit voltage and peak power density of ZABs employing different catalysts.

The structure and composition of $\text{Co}(\text{OH})_2/\text{CoPt}/\text{N-CN}$ before and after the cycling process were observed by XRD, XPS, and TEM measurements [17]. XRD patterns of $\text{Co}(\text{OH})_2/\text{CoPt}/\text{N-CN}$ suggested excellent stability during the charge–discharge process. However, the decreased binding energy of $\text{Pt } 4f_{5/2}$ during the charge–discharge process indicated that the electrocatalytic activity of $\text{Co}(\text{OH})_2/\text{CoPt}/\text{N-CN}$ was slightly diminished. Moreover, the binding energy of $\text{Co } 2p$ electrons shifted negatively, and the binding energy gap between $2p_{1/2}$ and $2p_{3/2}$ electrons decreased, confirming that part of the $\text{Co}(\text{OH})_2$ was gradually oxidized into Co_3O_4 in the anodic potential region. The porous texture of the carbon matrix in Co@NC was well preserved after a long-term test, and some small detached nanoparticles aggregated in the pores [65]. The reduction of $\text{Co } (111)$ peak in the XRD pattern of Co@NC suggested that the Co nanoparticles in Co@NC were partially corroded to a reduced crystalline size and detached from the electrodes during the discharge–charge process, leading to the loss of voltaic efficiency.

Tang et al. investigated the structure of $\text{Co}_2\text{Fe}_1@\text{NC-AC}$ after ZAB's long-term cycling process to clarify the reason for battery stability [71]. The TEM image revealed that the structure of $\text{Co}_2\text{Fe}_1@\text{NC-AC}$ composite was preserved after 750 charge–discharge cycles (125 h). XANES and EXAFS results proved that the chemical states, k -space, and R space of Co and Fe were nearly unchanged after the cycling test. Carbon coating on the surface protected Co_2Fe_1 particles from deteriorating during battery operation, and thus excellent cycling properties were obtained.

In situ XRD was employed to observe the chemical transformations inside a battery with a PCP-800 cathode under operating conditions, and the existence of two continuous diffractions at 44° and 54° related to carbon throughout the working process was detected [142]. On the other hand, batteries with a $\text{Pt}/\text{C} + \text{IrO}_2$ cathode showed no signal

change during the discharge process. These observations indicated that the reactions in zinc–air batteries with a PCP-800 cathode were completely reversible.

Wu et al. employed in situ XAFS to investigate Fe (Fe-N and Fe-M) structure change in Fe₂Ni₂N/Co@NCNT during the charge–discharge process [143]. The results suggested that Fe oxidation states were nearly stable, and the bond length and local coordination remained unchanged during the discharge step. It was then found that the local Fe environment changed, and Fe-N bonding had a higher degree of order than Fe-M bonding during the discharge step. EXAFS also revealed de-intercalation of some metal atoms from Fe₂Ni₂N/Co. Finally, a minor change of Fe₂Ni₂N/Co@NCNT slightly affected its catalytic activity.

Table 4. Performances of some typical ZABs.

Catalyst	Loading (mg cm ⁻²)	Polarization (ΔE/V)	Open Circuit Voltage (V)	Rechargeability (Cycle Number, 1st Charge/Discharge Voltages, Cycle Time/min)	Reference
RuSn	20	0.7	1.36	100, 1.9/1.2, 20	[25]
P,S-CNS	0.45	0.8	1.51	>500, 2.02/1.22, 12	[144]
PS-CNFs	0.20	0.81	1.49	600, 2.2/1.19, 12	[145]
CNT@POF	1.50	0.78	1.39	200, 1.99/1.21, 20	[146]
Fe(Co)-N _x /C	1.0	0.73	1.48	2000, 1.97/1.24, 20	[147]
DDPCN	n/a	0.9	1.48	360, 2.1/1.2, 5	[53]
CK-800-800	4	1.21	1.51	300, 2.41/ 1.2, 10	[148]
Fe–NCNS	1	0.7	1.49	1000, 1.90/1.2, 10	[149]
2D Fe-NG	1	0.91	1.51	480, 2.1/1.19, 10	[45]
Co-N-C	5	0.40	1.40	72, 1.75/1.35, 20	[40]
FeN _x -embedded PNC	8	0.8	1.55	300, 2.0/1.2, 10	[48]
E-CoSA/N/C	1	0.79	1.49	1000, 2.0/1.21, 10	[41]
Co–N–C nanobrushes	1	0.84	1.50	420, 2.05/1.21, 20	[150]
GNCNTs	1	0.8	1.48	9000, 1.9/1.1, 20	[37]
Co@NC-3	0.5	0.95	1.377	450, 2.2/1.25, 10	[63]
Co ₂ Fe ₁ @NC	2	0.75	1.45	750, 2.0/1.25, 10	[71]
Co@NC	1	0.74	1.46	300, 1.97/1.23, 10	[65]
FeCo@NC	1	0.7	1.38	200, 1.9/1.2, 10	[75]
CoFe@NCNTs	1	0.7	1.45	500, 1.9/1.2, 10	[77]
Ni ₃ Fe/N-S-CNTs	1	0.6	1.41	500, 1.85/1.25, 60	[85]
Fe _{1.2} Co@NC/NCNTs	2.0	0.74	1.43	300, 1.98/1.24, 10	[78]
FeCo-NC _{ps}	n/a	0.71	1.43	1400, 1.9/1.19, 6.7	[67]
Ni ₃ Fe/N-C	0.5	0.95	1.5	402, 2.05/1.1, 20	[80]
FeCo-N-C-700	3	0.46	1.39	240, 1.72/1.26, 10	[66]
NiFe@N-CFs	1.5	0.7	1.4	300, 1.92/1.26, 40	[151]
FeNi/N-CPCF	2.0	0.77	1.478	960, 1.99/1.22, 40	[84]
P–FeNi/NC@G	1.1	0.68	1.53	144, 1.9/1.18, 10	[152]
NiFe@NCNTs	n/a	0.6	1.48	2400, 1.9/1.3, 5	[83]
CoFe@NC/KB-800	0.5	0.5	1.44	600, 1.8/1.3, 10	[69]
Co–N _x /C	1.0	0.68	1.42	120, 1.93/1.25, 5	[153]
Ni/NiO nanosheets	2	0.73	1.47	720, 1.99/1.26, 10	[154]
Co@Co ₄ N/MnO-NC	2.5~3.0	0.87	1.47	2800, 2.14/1.27, 10	[155]
Fe _x Ni _y N@C/NC	2	0.9	1.25	400, 1.95/1.05, 60	[156]
NiFe LDH-CoPc/CNTs	n/a	0.67	1.40	550, 1.90/1.23, 120	[93]
NiCo ₂ O ₄ @NiMn LDH	2.0	0.92	1.40	500, 2.1/1.18, 10	[100]
Co ₃ O ₄ @NiFe LDHs	n/a	0.78	1.5	1250, 1.98/1.2, 10	[97]
MCN-LDH	3	1.0	1.4	430, 2/1, 16.7	[94]
MnO _x -NiFe LDH/Ni	n/a	0.7	1.4	660, 1.9/1.2, 10	[92]
CoNi-NS/rGO	1	0.81	1.37	350, 2.0/1.19, 1.67	[102]
NiCo ₂ O ₄ @FeNi LDH	n/a	0.65	1.40	90, 1.9/1.25, 60	[96]

Table 4. Cont.

Catalyst	Loading (mg cm ⁻²)	Polarization (ΔE/V)	Open Circuit Voltage (V)	Rechargeability (Cycle Number, 1st Charge/Discharge Voltages, Cycle Time/min)	Reference
NiFe LDH	1.20	0.85	n/a	600, 1.95/1.10, 10	[157]
CoMn-LDH/NPGA	n/a	0.83	1.514	432, 2.04/1.21, 10	[103]
Co ₉ S ₈ /S-rGO	10	0.65	1.42	150, 1.95/1.3, 20	[158]
S-GNS/NiCo ₂ S ₄	n/a	0.7	1.31	150, 1.9/1.2, 40	[159]
Co/S/N-800	1.0	0.65	1.54	72, 1.97/1.32, 40	[107]
CuCo ₂ S ₄ NSs@N-CNFs	n/a	0.9	1.46	300, 2.1/1.2, 20	[160]
FeCoMoS@NG	1	0.7	1.44	420, 1.95/1.25, 10	[112]
Co ₉ S ₈ /GN	2	0.55	1.41	30, 1.8/1.25, 10	[108]
Ni _{1-x} Mo _x OSe	1.5	0.73	1.429	300, 1.95/1.22, 60	[161]
FeS ₂ -CoS ₂ /NCFs	1.2	0.88	1.46	1500, 2.08/1.2, 10	[162]
Fe/N/C@BMZIF	1	0.82	1.48	100, 1.95/1.13, 10	[163]
Fe-N/C	2	1.0	1.525	50, 2.1/1.1, 10	[164]
Ni _{2.25} Co _{0.75} N/NrGO	2.85	0.75	1.43	500, 1.97/1.22, 20	[165]
Mn _x Fe _{3-x} C/NC	2	1.1	1.5	1000, 2.2/ 1.1, 20	[166]
Fe ₂ Ni ₂ N/Co@NCNT	2	0.75	1.3	850, 1.9/1.15, 60	[143]
CuSA@HNCN _x	0.5	0.65	1.51	1800, 1.95/1.3, 10	[167]
Co@WC _{1-x} /NCNTs	1.0	0.9	1.452	200, 2.0/1.1, 20	[168]
Zn-Ni ₃ FeN/NG	1	0.8	1.60	540, 1.95/1.15, 20	[141]
FeN _x C	0.5	0.65	1.41	600, 1.85/1.2, 10	[169]
TCoNCNTs + NiFe-LDH	2 + 1	0.7	1.39	100, 1.95/1.25, 50	[170]
NCO-250	1	0.77	1.51	225, 2.0/1.23, 20	[171]
Pd-La _{0.7} Sr _{0.3} CoO _{3-δ}	1	1.2	1.5	60, 2.2/ 1.0, 60	[172]
NP-Co ₃ O ₄ /CC	0.8	0.8	1.576	1200, 1.9/1.1, 20	[130]
MnO ₂ -Fe ₂ O ₃ /CNT	1.0	0.69	1.51	360, 1.95/1.26, 10	[173]
S-CoMn ₂ O ₄	1.0	0.8	1.52	180, 2.0/1.2, 20	[138]

9. Summary and Outlook

The atomic form of noble metals exhibits better ORR ability than the nanoparticle form. Alloy formation with transition metals (Fe, Co, Cu) stabilizes Pt and Ag at the atomic level and thus enhances ORR catalytic activity and stability. In addition, solid solution formation enhances the activity of RuO₂ in both ORR and OER. Nitrogen-doped carbon also exhibits good ORR capability, and the OER properties could be enhanced by co-doping with other elements or by mixing with an OER catalyst. Iron, cobalt, sulphur, and phosphorus enhance oxygen-related reactions when they exist in the NC skeleton in the form Co-N_x, Fe-N_x, C-S-C, P-O, P-C, or P-C-N. The combination of nitrogen-doped carbon materials and metal nanoparticles produces outstanding bifunctional catalysts. Co nanoparticles contributed to the ORR, while Fe-based nanoparticles improved the OER. Ni₃Fe/N-S-CNT and FeNi₃@NC exhibited catalytic properties comparable to those of noble metal catalysts. Transition metal chalcogenides exhibit high activity in the OER, and this could be enhanced by aliovalent substitution of the metal ion or oxygen doping. The formation of an interface between two chalcogenides increases their ORR activity and thus makes them binary catalysts. Layered double hydroxides (LDHs) have emerged as one of the most effective OER catalysts due to their excellent activity and stability in an OER under alkaline conditions, structural and compositional flexibility, ease of synthesis, and low cost. Metal oxide catalysts are highly desirable because of the abundance of the elements, the stability of the oxide in alkaline media, and their high economic efficiency; however, their catalytic activity is still far behind that of other compounds.

In general, noble metals and nitrogen-doped carbon exhibited catalytic activity in ORR, while LDHs, metal nanoparticles, and transition metal chalcogenides exhibited catalytic

activity in OER. Therefore, a bifunctional catalyst should consist of any two components from the two groups.

Zinc–air batteries show potential for application in both stationary energy storage and portable devices. The performance of a zinc–air battery strongly depends on the activity of a bifunctional catalyst. While there are many research papers reporting the preparation and activity of bifunctional catalysts for zinc–air batteries, their Coulomb efficiency and energy efficiency were still lower than 70%, which is still far from meeting practical requirements. Catalyst degradation is a significant challenge in obtaining a stable zinc–air battery. It was found that the detachment and irreversible oxidation of active components were the main reasons for cell failure and overvoltage of the charge–discharge process. In addition, the cycling time for most of the reported cells was very short, and there are few reports investigating structural changes after long-term testing. Therefore, more studies on the stability of zinc–air batteries are needed to boost their application.

Author Contributions: Writing—original draft preparation, N.H.H.P., T.A.T. and P.T.T.P.; writing—review and editing, L.C.L., C.X.V., N.T. and L.V.T. All authors have read and agreed to the published version of the manuscript.

Funding: This research received no external funding.

Acknowledgments: We acknowledge the support of time and facilities from Ho Chi Minh City University of Technology (HCMUT), VNU-HCM for this study.

Conflicts of Interest: The authors declare no conflict of interest.

References

1. Dunn, H.B.; Tarascon, J.-M. Electrical Energy Storage for the Grid: A Battery of Choices. *Science* **2011**, *334*, 928–935. [CrossRef] [PubMed]
2. Lee, J.-S.; Kim, S.T.; Cao, R.; Choi, N.-S.; Liu, M.; Lee, K.; Cho, J. Metal-Air Batteries with High Energy Density: Li-Air versus Zn-Air. *Adv. Energy Mater.* **2011**, *1*, 34–50. [CrossRef]
3. Lim, M.B.; Lambert, T.N. *Rechargeable Zinc Batteries for Grid Storage, 2020 U.S. DOE Energy Storage Handbook*; Sandia National Laboratory: Albuquerque, NM, USA, 2020. Available online: <http://www.sandia.gov/> (accessed on 30 January 2023).
4. Fu, J.; Cano, Z.; Park, M.; Yu, A.; Fowler, M.; Chen, Z. Electrically Rechargeable Zinc-Air Batteries: Progress, Challenges, and Perspectives. *Adv. Mater.* **2017**, *29*, 1604685. [CrossRef] [PubMed]
5. Akhil, G.A.A.; Currier, A.B.; Kaun, B.C.; Rastler, D.M.; Chen, S.B.; Cotter, A.L.; Bradshaw, D.T.; Gauntlett, W.D. *DOE/EPRI Electricity Storage Handbook in Collaboration with NRECA*; Sandia National Laboratory: Albuquerque, NM, USA, 2015. Available online: <http://www.osti.gov/bridge> (accessed on 30 January 2023).
6. Zhang, J.; Vukmirovic, M.; Xu, Y.; Mavrikakis, M.; Adzic, R. Controlling the Catalytic Activity of Platinum-Monolayer Electrocatalysts for Oxygen Reduction with Different Substrates. *Angew. Chem.* **2005**, *117*, 2170–2173. [CrossRef]
7. Borodzinski, G. Relation between the surface states of oxide films at Rh electrodes and kinetics of the oxygen evolution reaction. *J. Chem. Soc. Faraday Trans.* **1994**, *90*, 3669–3675.
8. Antolini, E. Iridium As Catalyst and Cocatalyst for Oxygen Evolution/Reduction in Acidic Polymer Electrolyte Membrane Electrolyzers and Fuel Cells. *ACS Catal.* **2014**, *4*, 1426–1440. [CrossRef]
9. Da Silva, M.G.C.; Ticianelli, E.A. Activity and Stability of Pt/IrO₂ Bifunctional Materials as Catalysts for the Oxygen Evolution/Reduction Reactions. *ACS Catal.* **2018**, *8*, 2081–2092. [CrossRef]
10. Ioroi, N.T.; Yasuda, K.; Yamamoto, Y.; Takenaka, H. Iridium Oxide/Platinum Electrocatalysts for Unitized Regenerative Polymer Electrolyte Fuel Cells. *J. Electrochem. Soc.* **2000**, *147*, 2018–2022. [CrossRef]
11. Zhang, Y.; Wang, C.; Wan, N.; Mao, Z. Deposited RuO₂–IrO₂/Pt electrocatalyst for the regenerative fuel cell. *Int. J. Hydrogen Energy* **2007**, *32*, 400–404. [CrossRef]
12. Spendelov, J.; Wieckowski, A. Electrocatalysis of oxygen reduction and small alcohol oxidation in alkaline media. *Phys. Chem. Chem. Phys.* **2007**, *9*, 2654–2675. [CrossRef]
13. Bak, J.; Kim, H.; Lee, S.; Kim, M.; Kim, E.-J.; Roh, J.; Shin, J.; Choi, C.; Cho, E. Boosting the Role of Ir in Mitigating Corrosion of Carbon Support by Alloying with Pt. *ACS Catal.* **2020**, *10*, 12300–12309. [CrossRef]
14. Islam, J.; Kim, S.-K.; Kim, K.-H.; Lee, E.; Park, G.-G. Enhanced durability of Pt/C catalyst by coating carbon black with silica for oxygen reduction reaction. *Int. J. Hydrogen Energy* **2021**, *46*, 1133–1143. [CrossRef]
15. Cui, Z.; Fu, G.; Li, Y.; Goodenough, J. Ni₃FeN-Supported Fe₃Pt Intermetallic Nanoalloy as a High-Performance Bifunctional Catalyst for Metal-Air Batteries. *Angew. Chem.* **2017**, *56*, 9901–9905. [CrossRef] [PubMed]

16. Zhong, X.; Ye, S.; Tang, J.; Zhu, Y.; Wu, D.; Gu, M.; Pan, H.; Xu, B. Engineering Pt and Fe dual-metal single atoms anchored on nitrogen-doped carbon with high activity and durability towards oxygen reduction reaction for zinc-air battery. *Appl. Catal. B Environ.* **2021**, *286*, 119891. [[CrossRef](#)]
17. Wang, K.; Wu, W.; Tang, Z.; Li, L.; Chen, S.; Bedford, N. Hierarchically Structured Co(OH)₂/CoPt/N-CN Air Cathodes for Rechargeable Zinc-Air Batteries. *ACS Appl. Mater. Interfaces* **2019**, *11*, 4983–4994. [[CrossRef](#)]
18. Li, Z.; Niu, W.; Yang, Z.; Zaman, N.; Samarakoon, W.; Wang, M.; Kara, A.; Lucero, M.; Vyas, M.; Cao, H.; et al. Stabilizing atomic Pt with trapped interstitial F in alloyed PtCo nanosheets for high-performance zinc-air batteries. *Energy Environ. Sci.* **2020**, *13*, 884–895. [[CrossRef](#)]
19. Su, Z.; Liu, X.; Hao, S.; Li, Z.; Yang, B.; Hou, Y.; Lei, L.; Zhang, X. Pt/CoFe₂O₄-C hollow ball as efficient bifunctional electrocatalyst for Zn-air batteries. *Catal. Today* **2021**, *368*, 204–210. [[CrossRef](#)]
20. Shinagawa, T.; Garcia-Esparza, A.; Takanabe, K. Insight on Tafel slopes from a microkinetic analysis of aqueous electrocatalysis for energy conversion. *Sci. Rep.* **2015**, *5*, 13801. [[CrossRef](#)]
21. Liang, Y.; Lei, H.; Wang, S.; Wang, Z.; Mai, W. Pt/Zn heterostructure as efficient air-electrocatalyst for long-life neutral Zn-air batteries. *Sci. China Mater.* **2021**, *64*, 1868–1875. [[CrossRef](#)]
22. Hu, J.; Liu, Q.; Shi, L.; Shi, Z.; Huang, H. Silver decorated LaMnO₃ nanorod/graphene composite electrocatalysts as reversible metal-air battery electrodes. *Appl. Surf. Sci.* **2017**, *402*, 61–69. [[CrossRef](#)]
23. Jin, Y.; Chen, F. Facile preparation of Ag-Cu bifunctional electrocatalysts for zinc-air batteries. *Electrochim. Acta* **2015**, *158*, 437–445. [[CrossRef](#)]
24. Wu, X.; Chen, F.; Zhang, N.; Qaseem, A.; Johnston, R. A silver–copper metallic glass electrocatalyst with high activity and stability comparable to Pt/C for zinc–air batteries. *J. Mater. Chem. A* **2016**, *4*, 3527–3537. [[CrossRef](#)]
25. You, T.; Hu, C. Designing Binary Ru-Sn Oxides with Optimized Performances for the Air Electrode of Rechargeable Zinc-Air Batteries. *ACS Appl. Mater. Interfaces* **2018**, *10*, 10064–10075. [[CrossRef](#)] [[PubMed](#)]
26. Gong, F.K.; Xia, Z.; Durstock, M.; Dai, L. Nitrogen-Doped Carbon Nanotube Arrays with High Electrocatalytic Activity for Oxygen Reduction. *Science* **2009**, *323*, 760–764. [[CrossRef](#)] [[PubMed](#)]
27. Wan, W.; Wang, Q.; Zhang, L.; Liang, H.-W.; Chen, P.; Yu, S.-H. N-, P- and Fe-tridoped nanoporous carbon derived from plant biomass: An excellent oxygen reduction electrocatalyst for zinc–air batteries. *J. Mater. Chem. A* **2016**, *4*, 8602–8609. [[CrossRef](#)]
28. Qian, Y.; Hu, Z.; Ge, X.; Yang, S.; Peng, Y.; Kang, Z.; Liu, Z.; Lee, J.; Zhao, D. A metal-free ORR/OER bifunctional electrocatalyst derived from metal-organic frameworks for rechargeable Zn-Air batteries. *Carbon* **2017**, *111*, 641–650. [[CrossRef](#)]
29. Jin, H.; Zhou, H.; Li, W.; Wang, Z.; Yang, J.; Xiong, Y.; He, D.; Chen, L.; Mu, S. In situ derived Fe/N/S-codoped carbon nanotubes from ZIF-8 crystals as efficient electrocatalysts for the oxygen reduction reaction and zinc–air batteries. *J. Mater. Chem. A* **2018**, *6*, 20093–20099. [[CrossRef](#)]
30. Wang, H.-F.; Tang, C.; Wang, B.; Li, B.-Q.; Cui, X.; Zhang, Q. Defect-rich carbon fiber electrocatalysts with porous graphene skin for flexible solid-state zinc–air batteries. *Energy Storage Mater.* **2018**, *15*, 124–130. [[CrossRef](#)]
31. Cheng, Y.; Wang, Y.; Wang, Q.; Liao, Z.; Zhang, N.; Guo, Y.; Xiang, Z. Hierarchically porous metal-free carbon with record high mass activity for oxygen reduction and Zn-air batteries. *J. Mater. Chem. A* **2019**, *7*, 9831–9836. [[CrossRef](#)]
32. Cai, X.; Xia, B.; Franklin, J.; Li, B.; Wang, X.; Wang, Z.; Chen, L.; Lin, J.; Lai, L.; Shen, Z. Free-standing vertically-aligned nitrogen-doped carbon nanotube arrays/graphene as air-breathing electrodes for rechargeable zinc–air batteries. *J. Mater. Chem. A* **2017**, *5*, 2488–2495. [[CrossRef](#)]
33. Kim, H.; Lee, K.; Woo, S.; Jung, Y. On the mechanism of enhanced oxygen reduction reaction in nitrogen-doped graphene nanoribbons. *Phys. Chem. Chem. Phys. PCCP* **2011**, *13*, 17505–17510. [[CrossRef](#)] [[PubMed](#)]
34. Wang, Y.Q.; Lei, Y.; Wang, Y.; Wang, Y.; Li, Y.; Wang, S. Pyridinic-N-Dominated Doped Defective Graphene as a Superior Oxygen Electrocatalyst for Ultrahigh-Energy-Density Zn–Air Batteries. *ACS Energy Lett.* **2018**, *3*, 1183–1191. [[CrossRef](#)]
35. Wang, C.; Xie, N.-H.; Zhang, Y.; Huang, Z.; Xia, K.; Wang, H.; Guo, S.; Xu, B.-Q.; Zhang, Y. Silk-Derived Highly Active Oxygen Electrocatalysts for Flexible and Rechargeable Zn–Air Batteries. *Chem. Mater.* **2019**, *31*, 1023–1029. [[CrossRef](#)]
36. Li, Y.; Chen, M.; Chu, M.; Wang, X.; Wang, Y.; Lin, X.; Cao, X. Mono-Doped Carbon Nanofiber Aerogel as a High-Performance Electrode Material for Rechargeable Zinc-Air Batteries. *ChemElectroChem* **2021**, *8*, 829–838. [[CrossRef](#)]
37. Xu, Y.; Deng, P.; Chen, G.; Chen, J.; Yan, Y.; Qi, K.; Liu, H.; Xia, B. 2D Nitrogen-Doped Carbon Nanotubes/Graphene Hybrid as Bifunctional Oxygen Electrocatalyst for Long-Life Rechargeable Zn–Air Batteries. *Adv. Funct. Mater.* **2019**, *30*, 1906081. [[CrossRef](#)]
38. Li, Z.; Jiang, G.; Deng, Y.; Liu, G.; Ren, D.; Zhang, Z.; Zhu, J.; Gao, R.; Jiang, Y.; Luo, D.; et al. Deep-Breathing Honeycomb-like Co-N_x-C Nanopolyhedron Bifunctional Oxygen Electrocatalysts for Rechargeable Zn-Air Batteries. *iScience* **2020**, *23*, 101404. [[CrossRef](#)] [[PubMed](#)]
39. Tang, C.; Wang, B.; Wang, H.; Zhang, Q. Defect Engineering toward Atomic Co-N_x-C in Hierarchical Graphene for Rechargeable Flexible Solid Zn-Air Batteries. *Adv. Mater.* **2017**, *29*, 1703185. [[CrossRef](#)]
40. Li, J.-C.; Wu, X.-T.; Chen, L.-J.; Li, N.; Liu, Z.-Q. Bifunctional MOF-derived Co-N-doped carbon electrocatalysts for high-performance zinc-air batteries and MFCs. *Energy* **2018**, *156*, 95–102. [[CrossRef](#)]
41. Liu, S.; Ji, H.; Wang, M.; Sun, H.; Liu, J.; Yan, C.; Qian, T. Atomic Metal Vacancy Modulation of Single-Atom Dispersed Co/N/C for Highly Efficient and Stable Air Cathode. *ACS Appl. Mater. Interfaces* **2020**, *12*, 15298–15304. [[CrossRef](#)]
42. Chen, J.; Li, W.; Xu, B. Nitrogen-rich Fe-N-C materials derived from polyacrylonitrile as highly active and durable catalysts for the oxygen reduction reaction in both acidic and alkaline electrolytes. *J. Colloid. Interface Sci.* **2017**, *502*, 44–51. [[CrossRef](#)]

43. Wang, C.; Li, Z.; Wang, L.; Niu, X.; Wang, S. Facile Synthesis of 3D Fe/N Codoped Mesoporous Graphene as Efficient Bifunctional Oxygen Electrocatalysts for Rechargeable Zn–Air Batteries. *ACS Sustain. Chem. Eng.* **2019**, *7*, 13873–13885. [[CrossRef](#)]
44. Luo, X.; Liu, Z.; Ma, Y.; Nan, Y.; Gu, Y.; Li, S.; Zhou, Q.; Mo, J. Biomass derived Fe,N-doped carbon material as bifunctional electrocatalysts for rechargeable Zn-air batteries. *J. Alloys Compd.* **2021**, *888*, 161464. [[CrossRef](#)]
45. Wang, C.; Liu, Y.; Li, Z.; Wang, L.; Niu, X.; Sun, P. Novel space-confinement synthesis of two-dimensional Fe, N-codoped graphene bifunctional oxygen electrocatalyst for rechargeable air-cathode. *Chem. Eng. J.* **2021**, *411*, 128492. [[CrossRef](#)]
46. Liu, J.; Zhu, Y.; Fan, C.; Wang, J.; Du, F.; Jiang, L. Three-Dimensional Porous Fe–N–C Derived from Iron-Citrate-Functionalized Melamine Foam as a Highly Active Oxygen Reduction Catalyst for Zn–Air Batteries. *Energy Technol.* **2020**, *8*, 2000149. [[CrossRef](#)]
47. Du, C.; Gao, Y.; Wang, J.; Chen, W. A new strategy for engineering a hierarchical porous carbon-anchored Fe single-atom electrocatalyst and the insights into its bifunctional catalysis for flexible rechargeable Zn–air batteries. *J. Mater. Chem. A* **2020**, *8*, 9981–9990. [[CrossRef](#)]
48. Ma, L.; Chen, S.; Pei, Z.; Huang, Y.; Liang, G.; Mo, F.; Yang, Q.; Su, J.; Gao, Y.; Zapien, J.; et al. Single-Site Active Iron-Based Bifunctional Oxygen Catalyst for a Compressible and Rechargeable Zinc-Air Battery. *ACS Nano* **2018**, *12*, 1949–1958. [[CrossRef](#)] [[PubMed](#)]
49. Ma, Z.; Wang, K.; Qiu, Y.; Liu, X.; Cao, C.; Feng, Y.; Hu, P. Nitrogen and sulfur co-doped porous carbon derived from bio-waste as a promising electrocatalyst for zinc-air battery. *Energy* **2018**, *143*, 43–55. [[CrossRef](#)]
50. Zhu, J.; Li, W.; Li, S.; Zhang, J.; Zhou, H.; Zhang, C.; Zhang, J.; Mu, S. Defective N/S-Codoped 3D Cheese-Like Porous Carbon Nanomaterial toward Efficient Oxygen Reduction and Zn-Air Batteries. *Small* **2018**, *14*, e1800563. [[CrossRef](#)]
51. Kim, M.-J.; Park, J.; Kim, S.; Lim, M.; Jin, A.; Kim, O.-H.; Kim, M.; Lee, K.-S.; Kim, J.; Kim, S.-S.; et al. Biomass-Derived Air Cathode Materials: Pore-Controlled S,N-Co-doped Carbon for Fuel Cells and Metal–Air Batteries. *ACS Catal.* **2019**, *9*, 3389–3398. [[CrossRef](#)]
52. Fan, H.; Wang, Y.; Gao, F.; Yang, L.; Liu, M.; Du, X.; Wang, P.; Yang, L.; Wu, Q.; Wang, X.; et al. Hierarchical sulfur and nitrogen co-doped carbon nanocages as efficient bifunctional oxygen electrocatalysts for rechargeable Zn-air battery. *J. Energy Chem.* **2019**, *34*, 64–71. [[CrossRef](#)]
53. Najam, T.; Shah, S.A.; Ali, H.; Song, Z.; Sun, H.; Peng, Z.; Cai, X. A metal free electrocatalyst for high-performance zinc-air battery applications with good resistance towards poisoning species. *Carbon* **2020**, *164*, 12–18. [[CrossRef](#)]
54. Chen, S.; Cui, M.; Yin, Z.; Zeng, Q.; Cao, Z.; Xiong, J.; Mi, L.; Li, Y. Confined Synthesis of N, P Co-Doped 3D Hierarchical Carbons as High-Efficiency Oxygen Reduction Reaction Catalysts for Zn–Air Battery. *ChemElectroChem* **2020**, *7*, 4131–4135. [[CrossRef](#)]
55. Li, Y.; Gong, M.; Liang, Y.; Feng, J.; Kim, J.; Wang, H.; Hong, G.; Zhang, B.; Dai, H. Advanced zinc-air batteries based on high-performance hybrid electrocatalysts. *Nat. Commun.* **2013**, *4*, 1805. [[CrossRef](#)] [[PubMed](#)]
56. Li, Y.; Dai, H. Recent advances in zinc-air batteries. *Chem. Soc. Rev.* **2014**, *43*, 5257–5275. [[CrossRef](#)] [[PubMed](#)]
57. Wang, H.-F.; Tang, C.; Zhang, Q. A Review of Precious-Metal-Free Bifunctional Oxygen Electrocatalysts: Rational Design and Applications in Zn–Air Batteries. *Adv. Funct. Mater.* **2018**, *28*, 1803329. [[CrossRef](#)]
58. Han, C.; Li, W.; Liu, H.-K.; Dou, S.; Wang, J. Design strategies for developing non-precious metal based bi-functional catalysts for alkaline electrolyte based zinc–air batteries. *Mater. Horiz.* **2019**, *6*, 1812–1827. [[CrossRef](#)]
59. Zhao, J.; Zhang, J.; Li, Z.; Bu, X. Recent Progress on NiFe-Based Electrocatalysts for the Oxygen Evolution Reaction. *Small* **2020**, *16*, e2003916. [[CrossRef](#)]
60. Wang, T.; Kou, Z.; Mu, S.; Liu, J.; He, D.; Amiin, I.; Meng, W.; Zhou, K.; Luo, Z.; Chaemchuen, S.; et al. 2D Dual-Metal Zeolitic-Imidazolate-Framework-(ZIF)-Derived Bifunctional Air Electrodes with Ultrahigh Electrochemical Properties for Rechargeable Zinc-Air Batteries. *Adv. Funct. Mater.* **2018**, *28*, 1705048. [[CrossRef](#)]
61. Li, H.; An, M.; Zhao, Y.; Pi, S.; Li, C.; Sun, W.; Wang, H.-G. Co nanoparticles encapsulated in N-doped carbon nanofibers as bifunctional catalysts for rechargeable Zn-air battery. *Appl. Surf. Sci.* **2019**, *478*, 560–566. [[CrossRef](#)]
62. Liu, L.; Wang, Y.; Yan, F.; Zhu, C.; Geng, B.; Chen, Y.; Chou, S. Cobalt-Encapsulated Nitrogen-Doped Carbon Nanotube Arrays for Flexible Zinc–Air Batteries. *Small Methods* **2019**, *4*, 1900571. [[CrossRef](#)]
63. Liu, Y.; Ji, D.; Li, M.; Xiao, J.; Dong, P.; Zhang, C.; Han, L.; Zhang, Y. Facile synthesis of cobalt nanoparticles encapsulated in nitrogen-doped carbon nanotubes for use as a highly efficient bifunctional catalyst in rechargeable Zn–Air batteries. *J. Alloys Compd.* **2020**, *842*, 155791. [[CrossRef](#)]
64. Shen, M.; Gao, K.; Duan, C.; Hu, W.; Ding, S.; Yang, G.; Ni, Y. Coordination-driven hierarchically structured composites with N-CNTs-grafted graphene-confined ultra-small Co nanoparticles as effective oxygen electrocatalyst in rechargeable Zn-air battery. *Ceram. Int.* **2021**, *47*, 30091–30098. [[CrossRef](#)]
65. Tan, M.; Xiao, Y.; Xi, W.; Lin, X.; Gao, B.; Chen, Y.; Zheng, Y.; Lin, B. Cobalt-nanoparticle impregnated nitrogen-doped porous carbon derived from Schiff-base polymer as excellent bifunctional oxygen electrocatalysts for rechargeable zinc-air batteries. *J. Power Sources* **2021**, *490*, 229570. [[CrossRef](#)]
66. Duan, X.; Ren, S.; Pan, N.; Zhang, M.; Zheng, H. MOF-derived Fe,Co@N–C bifunctional oxygen electrocatalysts for Zn–air batteries. *J. Mater. Chem. A* **2020**, *8*, 9355–9363. [[CrossRef](#)]
67. Liu, J.; He, T.; Wang, Q.; Zhou, Z.; Zhang, Y.; Wu, H.; Li, Q.; Zheng, J.; Sun, Z.; Lei, Y.; et al. Confining ultrasmall bimetallic alloys in porous N–carbon for use as scalable and sustainable electrocatalysts for rechargeable Zn–air batteries. *J. Mater. Chem. A* **2019**, *7*, 12451–12456. [[CrossRef](#)]

68. Fu, G.; Liu, Y.; Chen, Y.; Tang, Y.; Goodenough, J.; Lee, J. Robust N-doped carbon aerogels strongly coupled with iron-cobalt particles as efficient bifunctional catalysts for rechargeable Zn-air batteries. *Nanoscale* **2018**, *10*, 19937–19944. [[CrossRef](#)]
69. Ren, S.; Duan, X.; Ge, F.; Chen, Z.; Yang, Q.; Zhang, M.; Zheng, H. Novel MOF-derived hollow CoFe alloy coupled with N-doped Ketjen Black as boosted bifunctional oxygen catalysts for Zn-air batteries. *Chem. Eng. J.* **2022**, *427*, 131614. [[CrossRef](#)]
70. Hao, X.; Jiang, Z.; Zhang, B.; Tian, X.; Song, C.; Wang, L.; Maiyalagan, T.; Hao, X.; Jiang, Z.J. N-Doped Carbon Nanotubes Derived from Graphene Oxide with Embedment of FeCo Nanoparticles as Bifunctional Air Electrode for Rechargeable Liquid and Flexible All-Solid-State Zinc-Air Batteries. *Adv. Sci.* **2021**, *8*, 2004572. [[CrossRef](#)]
71. Tang, T.; Jiang, W.; Liu, X.; Deng, J.; Niu, S.; Wang, B.; Jin, S.; Zhang, Q.; Gu, L.; Hu, J.; et al. Metastable Rock Salt Oxide-Mediated Synthesis of High-Density Dual-Protected M@NC for Long-Life Rechargeable Zinc-Air Batteries with Record Power Density. *J. Am. Chem. Soc.* **2020**, *142*, 7116–7127. [[CrossRef](#)]
72. Wang, M.; Liu, Y.; Zhang, K.; Yu, F.; Qin, F.; Fang, J.; Lai, Y.; Li, J. Metal coordination enhanced Ni-Co@N-doped porous carbon core-shell microsphere bi-functional electrocatalyst and its application in rechargeable zinc/air batteries. *RSC Adv.* **2016**, *6*, 83386–83392. [[CrossRef](#)]
73. Deng, Z.; Yi, Q.; Li, G.; Chen, Y.; Yang, X.; Nie, H. NiCo-doped C-N nano-composites for cathodic catalysts of Zn-air batteries in neutral media. *Electrochim. Acta* **2018**, *279*, 1–9. [[CrossRef](#)]
74. Asokan, A.; Lee, H.; Gwon, O.; Kim, J.; Kwon, O.; Kim, G. Insights Into the Effect of Nickel Doping on ZIF-Derived Oxygen Reduction Catalysts for Zinc–Air Batteries. *ChemElectroChem* **2019**, *6*, 1213–1224. [[CrossRef](#)]
75. Cai, P.; Ci, S.; Zhang, E.; Shao, P.; Cao, C.; Wen, Z. FeCo Alloy Nanoparticles Confined in Carbon Layers as High-activity and Robust Cathode Catalyst for Zn-Air Battery. *Electrochim. Acta* **2016**, *220*, 354–362. [[CrossRef](#)]
76. Ma, Y.; Zang, W.; Sumboja, A.; Mao, L.; Liu, X.; Tan, M.; Pennycook, S.; Kou, Z.; Liu, Z.; Li, X.; et al. Hollow structure engineering of FeCo alloy nanoparticles electrospun in nitrogen-doped carbon enables high performance flexible all-solid-state zinc-air batteries. *Sustain. Energy Fuels* **2020**, *4*, 1747–1753. [[CrossRef](#)]
77. Cai, P.; Hong, Y.; Ci, S.; Wen, Z. In situ integration of CoFe alloy nanoparticles with nitrogen-doped carbon nanotubes as advanced bifunctional cathode catalysts for Zn-air batteries. *Nanoscale* **2016**, *8*, 20048–20055. [[CrossRef](#)] [[PubMed](#)]
78. Li, S.; Chen, W.; Pan, H.; Cao, Y.; Jiang, Z.; Tian, X.; Hao, X.; Maiyalagan, T.; Jiang, Z.-J. FeCo Alloy Nanoparticles Coated by an Ultrathin N-Doped Carbon Layer and Encapsulated in Carbon Nanotubes as a Highly Efficient Bifunctional Air Electrode for Rechargeable Zn-Air Batteries. *ACS Sustain. Chem. Eng.* **2019**, *7*, 8530–8541. [[CrossRef](#)]
79. Corrigan, D. The Catalysis of the Oxygen Evolution Reaction by Iron Impurities in Thin Film Nickel Oxide Electrodes. *J. Electrochem. Soc.* **1987**, *134*, 377–384. [[CrossRef](#)]
80. Sun, P.; Zuo, Z.; He, M.; Yang, L.; Zhang, D.; Huang, N.; Chen, Z.; Sun, Y.; Sun, X. N-doped carbon sheets loaded with well-dispersed Ni₃Fe nanoparticles as bifunctional oxygen electrode for rechargeable Zn-air battery. *J. Electroanal. Chem.* **2019**, *851*, 113418. [[CrossRef](#)]
81. Hao, X.; Jiang, Z.; Tian, X.; Song, C.; Chen, S.; Hao, X.; Jiang, Z.-J.; Ultrasml, S. Homogeneously Distributed Ni₃Fe Alloy Nanoparticles on N-Doped Porous Graphene as a Bifunctional Electrocatalyst for Rechargeable Flexible Solid Zinc-Air Batteries. *ACS Appl. Energy Mater.* **2020**, *3*, 12148–12161. [[CrossRef](#)]
82. Chen, K.; Kim, S.; Rajendiran, R.; Prabakar, K.; Li, G.; Shi, Z.; Jeong, C.; Kang, J.; Li, O. Enhancing ORR/OER active sites through lattice distortion of Fe-enriched FeNi₃ intermetallic nanoparticles doped N-doped carbon for high-performance rechargeable Zn-air battery. *J. Colloid Interface Sci.* **2021**, *582*, 977–990. [[CrossRef](#)]
83. Jiang, M.; Tan, Z.; Cao, M. A robust bifunctional electrocatalyst for rechargeable zinc-air batteries: NiFe nanoparticles encapsulated in nitrogen-doped carbon nanotubes. *Int. J. Hydrogen Energy* **2021**, *46*, 15507–15516. [[CrossRef](#)]
84. Wang, Z.; Ang, J.; Liu, J.; Ma, X.; Kong, J.; Zhang, Y.; Yan, T.; Lu, X. FeNi alloys encapsulated in N-doped CNTs-tangled porous carbon fibers as highly efficient and durable bifunctional oxygen electrocatalyst for rechargeable zinc-air battery. *Appl. Catal. B Environ.* **2020**, *263*, 118344. [[CrossRef](#)]
85. Lai, C.; Wang, J.; Lei, W.; Xuan, C.; Xiao, W.; Zhao, T.; Huang, T.; Chen, L.; Zhu, Y.; Wang, D. Restricting Growth of Ni₃Fe Nanoparticles on Heteroatom-Doped Carbon Nanotube/Graphene Nanosheets as Air-Electrode Electrocatalyst for Zn-Air Battery. *ACS Appl. Mater. Interfaces* **2018**, *10*, 38093–38100. [[CrossRef](#)] [[PubMed](#)]
86. Bukhtiyarova, M. A review on effect of synthesis conditions on the formation of layered double hydroxides. *J. Solid State Chem.* **2019**, *269*, 494–506. [[CrossRef](#)]
87. Yang, Z.-z.; Zhang, C.; Zeng, G.-M.; Tan, X.-F.; Huang, D.-L.; Zhou, J.-W.; Fang, Q.-Z.; Yang, K.-H.; Wang, H.; Wei, J.; et al. State-of-the-art progress in the rational design of layered double hydroxide based photocatalysts for photocatalytic and photo-electrochemical H₂/O₂ production. *Coord. Chem. Rev.* **2021**, *446*, 214103. [[CrossRef](#)]
88. Gao, R.; Zhu, J.; Yan, D. Transition metal-based layered double hydroxides for photo(electro)chemical water splitting: A mini review. *Nanoscale* **2021**, *13*, 13593–13603. [[CrossRef](#)]
89. Yi, H.; Liu, S.; Lai, C.; Zeng, G.; Li, M.; Liu, X.; Li, B.; Huo, X.; Qin, L.; Li, L.; et al. Recent Advance of Transition-Metal-Based Layered Double Hydroxide Nanosheets: Synthesis, Properties, Modification, and Electrocatalytic Applications. *Adv. Energy Mater.* **2021**, *11*, 2002863. [[CrossRef](#)]
90. Yang, L.; Liu, Z.; Zhu, S.; Feng, L.; Xing, W. Ni-based layered double hydroxide catalysts for oxygen evolution reaction. *Mater. Today Phys.* **2020**, *16*, 100292. [[CrossRef](#)]

91. Wang, P.; Lin, Y.; Wan, L.; Wang, B. Construction of a Janus MnO₂-NiFe Electrode via Selective Electrodeposition Strategy as a High-Performance Bifunctional Electrocatalyst for Rechargeable Zinc-Air Batteries. *ACS Appl. Mater. Interfaces* **2019**, *11*, 37701–37707. [[CrossRef](#)]
92. Wan, L.; Wang, P.; Lin, Y.; Wang, B. Janus-Typed Integrated Bifunctional Air Electrode with MnO_x-NiFe LDH/Ni Foam for Rechargeable Zinc-Air Batteries. *J. Electrochem. Soc.* **2019**, *166*, A3409–A3415. [[CrossRef](#)]
93. Zhang, Z.; Zhou, D.; Zhou, L.; Yu, H.; Huang, B. NiFe LDH-CoPc/CNTs as novel bifunctional electrocatalyst complex for zinc-air battery. *Ionics* **2017**, *24*, 1709–1714. [[CrossRef](#)]
94. Qian, Y.; An, T.; Sarnello, E.; Liu, Z.; Li, T.; Zhao, D. Janus Electrocatalysts Containing MOF-Derived Carbon Networks and NiFe-LDH Nanoplates for Rechargeable Zinc-Air Batteries. *ACS Appl. Energy Mater.* **2019**, *2*, 1784–1792. [[CrossRef](#)]
95. Chen, D.; Chen, X.; Cui, Z.; Li, G.; Han, B.; Zhang, Q.; Sui, J.; Dong, H.; Yu, J.; Yu, L.; et al. Dual-active-site hierarchical architecture containing NiFe-LDH and ZIF-derived carbon-based framework composite as efficient bifunctional oxygen electrocatalysts for durable rechargeable Zn-air batteries. *Chem. Eng. J.* **2020**, *399*, 125718. [[CrossRef](#)]
96. Wan, L.; Zhao, Z.; Chen, X.; Liu, P.-F.; Wang, P.; Xu, Z.; Lin, Y.; Wang, B. Controlled Synthesis of Bifunctional NiCo₂O₄@FeNi LDH Core-Shell Nanoarray Air Electrodes for Rechargeable Zinc-Air Batteries. *ACS Sustain. Chem. Eng.* **2020**, *8*, 11079–11087. [[CrossRef](#)]
97. Guo, X.; Hu, X.; Wu, D.; Jing, C.; Liu, W.; Ren, Z.; Zhao, Q.; Jiang, X.; Xu, C.; Zhang, Y.; et al. Tuning the Bifunctional Oxygen Electrocatalytic Properties of Core-Shell Co₃O₄@NiFe LDH Catalysts for Zn-Air Batteries: Effects of Interfacial Cation Valences. *ACS Appl. Mater. Interfaces* **2019**, *11*, 21506–21514. [[CrossRef](#)]
98. Feng, X.; Jiao, Q.; Chen, W.; Dang, Y.; Dai, Z.; Suib, S.; Zhang, J.; Zhao, Y.; Li, H.; Feng, C. Cactus-like NiCo₂S₄@NiFe LDH hollow spheres as an effective oxygen bifunctional electrocatalyst in alkaline solution. *Appl. Catal. B: Environ.* **2021**, *286*, 119869. [[CrossRef](#)]
99. Sumboja, A.; Chen, J.; Zong, Y.; Lee, P.; Liu, Z. NiMn layered double hydroxides as efficient electrocatalysts for the oxygen evolution reaction and their application in rechargeable Zn-air batteries. *Nanoscale* **2017**, *9*, 774–780. [[CrossRef](#)]
100. Guo, X.; Zheng, T.; Ji, G.; Hu, N.; Xu, C.; Zhang, Y. Core/shell design of efficient electrocatalysts based on NiCo₂O₄ nanowires and NiMn LDH nanosheets for rechargeable zinc-air batteries. *J. Mater. Chem. A* **2018**, *6*, 10243–10252. [[CrossRef](#)]
101. Li, K.; Guo, D.; Kang, J.; Wei, B.; Zhang, X.; Chen, Y. Hierarchical Hollow Spheres Assembled with Ultrathin CoMn Double Hydroxide Nanosheets as Trifunctional Electrocatalyst for Overall Water Splitting and Zn Air Battery. *ACS Sustain. Chem. Eng.* **2018**, *6*, 14641–14651. [[CrossRef](#)]
102. Wang, T.; Wu, J.; Liu, Y.; Cui, X.; Ding, P.; Deng, J.; Zha, C.; Coy, E.; Li, Y. Scalable preparation and stabilization of atomic-thick CoNi layered double hydroxide nanosheets for bifunctional oxygen electrocatalysis and rechargeable zinc-air batteries. *Energy Storage Mater.* **2019**, *16*, 24–30. [[CrossRef](#)]
103. Zhang, G.; Xing, J.; Zhao, Y.; Yang, F. Hierarchical N,P co-doped graphene aerogels framework assembling vertically grown CoMn-LDH nanosheets as efficient bifunctional electrocatalyst for rechargeable Zinc-air battery. *J. Colloid. Interface Sci.* **2021**, *590*, 476–486. [[CrossRef](#)] [[PubMed](#)]
104. Ataca, C.; Şahin, H.; Ciraci, S. Stable, Single-Layer MX₂ Transition-Metal Oxides and Dichalcogenides in a Honeycomb-Like Structure. *J. Phys. Chem. C* **2012**, *116*, 8983–8999. [[CrossRef](#)]
105. Geng, N.-N.D.; Hor, T.S.A.; Chien, S.W.; Liu, Z.; Zong, Y. Cobalt Sulfide Nanoparticles Impregnated Nitrogen and Sulfur co-Doped Graphene as Bifunctional Catalyst for Rechargeable Zn-air Batteries. *RSC Adv.* **2015**, *5*, 7280–7284. [[CrossRef](#)]
106. Niu, W.; Li, Z.; Marcus, K.; Zhou, L.; Li, Y.; Ye, R.; Liang, K.; Yang, Y. Surface-Modified Porous Carbon Nitride Composites as Highly Efficient Electrocatalyst for Zn-Air Batteries. *Adv. Energy Mater.* **2018**, *8*, 1701642. [[CrossRef](#)]
107. Jia, N.; Liu, J.; Gao, Y.; Chen, P.; Chen, X.; An, Z.; Li, X.; Chen, Y. Graphene-Encapsulated Co₉S₈ Nanoparticles on N,S-Codoped Carbon Nanotubes: An Efficient Bifunctional Oxygen Electrocatalyst. *ChemSusChem* **2019**, *12*, 3390–3400. [[CrossRef](#)]
108. Sun, X.; Gong, Q.; Liang, Y.; Wu, M.; Xu, N.; Gong, P.; Sun, S.; Qiao, J. Exploiting a High-Performance "Double-Carbon" Structure Co₉S₈/GN Bifunctional Catalysts for Rechargeable Zn-Air Batteries. *ACS Appl. Mater. Interfaces* **2020**, *12*, 38202–38210. [[CrossRef](#)]
109. Liu, T.; Yang, F.; Cheng, G.; Luo, W. Reduced Graphene Oxide-Wrapped Co₉-xFe_xS₈/Co,Fe-N-C Composite as Bifunctional Electrocatalyst for Oxygen Reduction and Evolution. *Small* **2018**, *14*, 1703748. [[CrossRef](#)] [[PubMed](#)]
110. Jiang, T.; Dai, P.; Zhang, W.; Wu, M. Fish bone-derived N, S co-doped interconnected carbon nanofibers network coupled with (Fe, Co, Ni)₉S₈ nanoparticles as efficient bifunctional electrocatalysts for rechargeable and flexible all-solid-state Zn-air battery. *Electrochimica Acta* **2021**, *373*, 137903. [[CrossRef](#)]
111. Chen, L.; Cui, L.; Wang, Z.; He, X.; Zhang, W.; Asefa, T. Co₈FeS₈/N,S-Doped Carbons Derived from Fe-Co/S-Bridged Polyphthalocyanine: Efficient Dual-Function Air-Electrode Catalysts for Rechargeable Zn-Air Batteries. *ACS Sustain. Chem. Eng.* **2020**, *8*, 13147–13158. [[CrossRef](#)]
112. Ramakrishnan, S.; Balamurugan, J.; Vinothkannan, M.; Kim, A.; Sengodan, S.; Yoo, D. Nitrogen-doped graphene encapsulated FeCoMoS nanoparticles as advanced trifunctional catalyst for water splitting devices and zinc-air batteries. *Appl. Catal. B Environ.* **2020**, *279*, 119381. [[CrossRef](#)]
113. Zheng, X.; Han, X.; Liu, H.; Chen, J.; Fu, D.; Wang, J.; Zhong, C.; Deng, Y.; Hu, W. Controllable Synthesis of Ni_xSe (0.5 ≤ x ≤ 1) Nanocrystals for Efficient Rechargeable Zinc-Air Batteries and Water Splitting. *ACS Appl. Mater. Interfaces* **2018**, *10*, 13675–13684. [[CrossRef](#)] [[PubMed](#)]

114. Hu, G.; Fung, V.; Sang, X.; Unocic, R.; Ganesh, P. Superior electrocatalytic hydrogen evolution at engineered non-stoichiometric two-dimensional transition metal dichalcogenide edges. *J. Mater. Chem. A* **2019**, *7*, 18357–18364. [[CrossRef](#)]
115. Zheng, X.; Zhang, J.; Wang, J.; Zhang, Z.; Hu, W.; Han, Y. Facile synthesis of nickel cobalt selenide hollow nanospheres as efficient bifunctional electrocatalyst for rechargeable Zn-air battery. *Sci. China Mater.* **2019**, *63*, 347–355. [[CrossRef](#)]
116. Cao, Y.; Zheng, X.; Zhang, H.; Zhang, J.; Han, X.; Zhong, C.; Hu, W.; Deng, Y. Interface engineering of NiS₂/CoS₂ nanohybrids as bifunctional electrocatalysts for rechargeable solid state Zn-air battery. *J. Power Sources* **2019**, *437*, 226893. [[CrossRef](#)]
117. Yin, J.; Li, Y.; Lv, F.; Lu, M.; Sun, K.; Wang, W.; Wang, L.; Cheng, F.; Li, Y.; Xi, P.; et al. Oxygen Vacancies Dominated NiS₂/CoS₂ Interface Porous Nanowires for Portable Zn-Air Batteries Driven Water Splitting Devices. *Adv. Mater.* **2017**, *29*, 1704681. [[CrossRef](#)] [[PubMed](#)]
118. Guo, L.; Deng, J.; Wang, G.; Hao, Y.; Bi, K.; Wang, X.; Yang, Y. P-doped CoS₂ Embedded in TiO₂ Nanoporous Films for Zn-Air Batteries. *Adv. Funct. Mater.* **2018**, *28*, 1804540. [[CrossRef](#)]
119. Wang, X.; Sebastian, P.; Smit, M.; Yang, H.; Gamboa, S. Studies on the oxygen reduction catalyst for zinc-air battery electrode. *J. Power Sources* **2003**, *124*, 278–284. [[CrossRef](#)]
120. Ma, B.H. A bifunctional electrocatalyst α -MnO₂-LaNiO₃/carbon nanotubes composite for rechargeable zinc-air batteries. *RSC Adv.* **2014**, *4*, 46084–46092. [[CrossRef](#)]
121. Li, P.-C.; Hu, C.-C.; Lee, T.-C.; Chang, W.-S.; Wang, T. Synthesis and characterization of carbon black/manganese oxide air cathodes for zinc-air batteries. *J. Power Sources* **2014**, *269*, 88–97. [[CrossRef](#)]
122. Sumboja, A.; Ge, X.; Goh, F.; Li, B.; Geng, D.; Hor, T.; Zong, Y.; Liu, Z. Manganese Oxide Catalyst Grown on Carbon Paper as an Air Cathode for High-Performance Rechargeable Zinc-Air Batteries. *Chempluschem* **2015**, *80*, 1341–1346. [[CrossRef](#)]
123. Zhou, Q.; Hou, S.; Cheng, Y.; Sun, R.; Shen, W.; Tian, R.; Yang, J.; Pang, H.; Xu, L.; Huang, K.; et al. Interfacial engineering Co and MnO within N,S co-doped carbon hierarchical branched superstructures toward high-efficiency electrocatalytic oxygen reduction for robust Zn-air batteries. *Appl. Catal. B Environ.* **2021**, *295*, 120281. [[CrossRef](#)]
124. Zhong, Y.; Dai, J.; Xu, X.; Su, C.; Shao, Z. Facilitating Oxygen Redox on Manganese Oxide Nanosheets by Tuning Active Species and Oxygen Defects for Zinc-Air Batteries. *ChemElectroChem* **2020**, *7*, 4949–4955. [[CrossRef](#)]
125. Singh, S.; Dhavale, V.; Kurungot, S. Surface-Tuned Co₃O₄ Nanoparticles Dispersed on Nitrogen-Doped Graphene as an Efficient Cathode Electrocatalyst for Mechanical Rechargeable Zinc-Air Battery Application. *ACS Appl. Mater. Interfaces* **2015**, *7*, 21138–21149. [[CrossRef](#)] [[PubMed](#)]
126. Guan, C.; Sumboja, A.; Wu, H.; Ren, W.; Liu, X.; Zhang, H.; Liu, Z.; Cheng, C.; Pennycook, S.; Wang, J. Hollow Co₃O₄ Nanosphere Embedded in Carbon Arrays for Stable and Flexible Solid-State Zinc-Air Batteries. *Adv. Mater.* **2017**, *29*, 1704117. [[CrossRef](#)]
127. Ren, J.-T.; Yuan, G.-G.; Weng, C.-C.; Yuan, Z.-Y. Rationally Designed Co₃O₄-C Nanowire Arrays on Ni Foam Derived From Metal Organic Framework as Reversible Oxygen Evolution Electrodes with Enhanced Performance for Zn-Air Batteries. *ACS Sustain. Chem. Eng.* **2017**, *6*, 707–718. [[CrossRef](#)]
128. Chong, Y.; Pan, Z.; Su, M.; Yang, X.; Ye, D.; Qiu, Y. 1D/2D hierarchical Co_{1-x}Fe_xO@N-doped carbon nanostructures for flexible zinc-air batteries. *Electrochim. Acta* **2020**, *363*, 137264. [[CrossRef](#)]
129. Huang, K.; Wang, R.; Zhao, S.; Du, P.; Wang, H.; Wei, H.; Long, Y.; Deng, B.; Lei, M.; Ge, B.; et al. Atomic species derived CoO_x clusters on nitrogen doped mesoporous carbon as advanced bifunctional electro-catalysts for Zn-air battery. *Energy Storage Mater.* **2020**, *29*, 156–162. [[CrossRef](#)]
130. Wang, X.; Liao, Z.; Fu, Y.; Neumann, C.; Turchanin, A.; Nam, G.; Zschech, E.; Cho, J.; Zhang, J.; Feng, X. Confined growth of porous nitrogen-doped cobalt oxide nanoarrays as bifunctional oxygen electrocatalysts for rechargeable zinc-air batteries. *Energy Storage Mater.* **2020**, *26*, 157–164. [[CrossRef](#)]
131. Wang, C.-C.; Hung, K.-Y.; Ko, T.-E.; Hosseini, S.; Li, Y.-Y. Carbon-nanotube-grafted and nano-Co₃O₄-doped porous carbon derived from metal-organic framework as an excellent bifunctional catalyst for zinc-air battery. *J. Power Sources* **2020**, *452*, 227841. [[CrossRef](#)]
132. Prabu, M.; Ketpang, K.; Shanmugam, S. Hierarchical nanostructured NiCo₂O₄ as an efficient bifunctional non-precious metal catalyst for rechargeable zinc-air batteries. *Nanoscale* **2014**, *6*, 3173–3181.
133. Prabu, M.; Ramakrishnan, P.; Shanmugam, S. CoMn₂O₄ nanoparticles anchored on nitrogen-doped graphene nanosheets as bifunctional electrocatalyst for rechargeable zinc-Air battery. *Electrochem. Commun.* **2014**, *41*, 59–63. [[CrossRef](#)]
134. Lee, D.; Park, M.; Park, H.; Seo, M.; Ismayilov, V.; Ahmed, R.; Chen, Z. Highly active Co-doped LaMnO₃ perovskite oxide and N-doped carbon nanotube hybrid bi-functional catalyst for rechargeable zinc-Air batteries. *Electrochem. Commun.* **2015**, *60*, 38–41. [[CrossRef](#)]
135. Kosasang, S.; Gatemala, H.; Ma, N.; Chomkhuntod, P.; Sawangphruk, M. Trimetallic Spinel-Type Cobalt Nickel-Doped Manganese Oxides as Bifunctional Electrocatalysts for Zn-Air Batteries. *Batter. Supercaps* **2020**, *3*, 631–637. [[CrossRef](#)]
136. Li, S.; Zhou, X.; Fang, G.; Xie, G.; Liu, X.; Lin, X.; Qiu, H.-J. Multicomponent Spinel Metal Oxide Nanocomposites as High-Performance Bifunctional Catalysts in Zn-Air Batteries. *ACS Appl. Energy Mater.* **2020**, *3*, 7710–7718. [[CrossRef](#)]
137. Ran, J.; Wang, T.; Zhang, J.; Liu, Y.; Xu, C.; Xi, S.; Gao, D. Modulation of Electronics of Oxide Perovskites by Sulfur Doping for Electrocatalysis in Rechargeable Zn-Air Batteries. *Chem. Mater.* **2020**, *32*, 3439–3446. [[CrossRef](#)]
138. Zhang, Z.; Sun, H.; Li, J.; Shi, Z.; Fan, M.; Bian, H.; Wang, T.; Gao, D. S-doped CoMn₂O₄ with more high valence metallic cations and oxygen defects for zinc-air batteries. *J. Power Sources* **2021**, *491*, 229584. [[CrossRef](#)]

139. Chen, D.; Zhu, J.; Mu, X.; Cheng, R.; Li, W.; Liu, S.; Pu, Z.; Lin, C.; Mu, S. Nitrogen-Doped carbon coupled FeNi₃ intermetallic compound as advanced bifunctional electrocatalyst for OER, ORR and zn-air batteries. *Appl. Catal. B Environ.* **2020**, *268*, 118729. [[CrossRef](#)]
140. Yu, P.; Wang, L.; Sun, F.; Xie, Y.; Liu, X.; Ma, J.; Wang, X.; Tian, C.; Li, J.; Fu, H. Co Nanoislands Rooted on Co-N-C Nanosheets as Efficient Oxygen Electrocatalyst for Zn-Air Batteries. *Adv. Mater.* **2019**, *31*, e1901666. [[CrossRef](#)]
141. He, X.; Tian, Y.; Huang, Z.; Xu, L.; Wu, J.; Qian, J.; Zhang, J.; Li, H. Engineering the electronic states of Ni₃FeN via zinc ion regulation for promoting oxygen electrocatalysis in rechargeable Zn—Air batteries. *J. Mater. Chem. A* **2021**, *9*, 2301–2307. [[CrossRef](#)]
142. Ji, H.; Wang, M.; Liu, S.; Sun, H.; Liu, J.; Qian, T.; Yan, C. Pyridinic and graphitic nitrogen-enriched carbon paper as a highly active bifunctional catalyst for Zn-air batteries. *Electrochim. Acta* **2020**, *334*, 135562. [[CrossRef](#)]
143. Wu, M.; Zhang, G.; Qiao, J.; Chen, N.; Chen, W.; Sun, S. Ultra-long life rechargeable zinc-air battery based on high-performance trimetallic nitride and NCNT hybrid bifunctional electrocatalysts. *Nano Energy* **2019**, *61*, 86–95. [[CrossRef](#)]
144. Shinde, S.; Lee, C.; Sami, A.; Kim, D.; Lee, S.; Lee, J. Scalable 3-D Carbon Nitride Sponge as an Efficient Metal-Free Bifunctional Oxygen Electrocatalyst for Rechargeable Zn-Air Batteries. *ACS Nano* **2017**, *11*, 347–357. [[CrossRef](#)]
145. Shinde, S.; Yu, J.; Song, J.; Nam, Y.; Kim, D.; Lee, J. Highly active and durable carbon nitride fibers as metal-free bifunctional oxygen electrodes for flexible Zn-air batteries. *Nanoscale Horiz* **2017**, *2*, 333–341. [[CrossRef](#)]
146. Li, B.-Q.; Zhang, S.-Y.; Wang, B.; Xia, Z.-J.; Tang, C.; Zhang, Q. A porphyrin covalent organic framework cathode for flexible Zn—air batteries. *Energy Environ. Sci.* **2018**, *11*, 1723–1729. [[CrossRef](#)]
147. Dinh, K.; Pei, Z.; Yuan, Z.; Hoang, V.; Wei, L.; Huang, Q.; Liao, X.; Liu, C.; Chen, Y.; Yan, Q. The on-demand engineering of metal-doped porous carbon nanofibers as efficient bifunctional oxygen catalysts for high-performance flexible Zn—air batteries. *J. Mater. Chem. A* **2020**, *8*, 7297–7308. [[CrossRef](#)]
148. Qiao, Y.; Kong, F.; Zhang, C.; Li, R.; Kong, A.; Shan, Y. Highly efficient oxygen electrode catalyst derived from chitosan biomass by molten salt pyrolysis for zinc-air battery. *Electrochim. Acta* **2020**, *339*, 135923. [[CrossRef](#)]
149. Wang, M.; Ji, H.; Liu, S.; Sun, H.; Liu, J.; Yan, C.; Qian, T. Single-atom scale metal vacancy engineering in heteroatom-doped carbon for rechargeable zinc-air battery with reduced overpotential. *Chem. Eng. J.* **2020**, *393*, 124702. [[CrossRef](#)]
150. Luo, H.; Jiang, W.; Niu, S.; Zhang, X.; Zhang, Y.; Yuan, L.; He, C.; Hu, J. Self-Catalyzed Growth of Co-N-C Nanobrushes for Efficient Rechargeable Zn-Air Batteries. *Small* **2020**, *16*, e2001171. [[CrossRef](#)]
151. Niu, Y.; Teng, X.; Gong, S.; Chen, Z. A bimetallic alloy anchored on biomass-derived porous N-doped carbon fibers as a self-supporting bifunctional oxygen electrocatalyst for flexible Zn—Air batteries. *J. Mater. Chem. A* **2020**, *8*, 13725–13734. [[CrossRef](#)]
152. Yang, X.; Wu, X.; Guo, Z.; Li, Q.; Wang, H.; Ke, C.; Zeng, W.; Qiu, X.; He, Y.; Liang, X.; et al. Phosphorus/nitrogen co-doped and bimetallic MOF-derived cathode for all-solid-state rechargeable zinc—Air batteries. *RSC Adv.* **2020**, *10*, 33327–33333. [[CrossRef](#)]
153. Amiin, I.; Liu, X.; Pu, Z.; Li, W.; Li, Q.; Zhang, J.; Tang, H.; Zhang, H.; Mu, S. From 3D ZIF Nanocrystals to Co-N_x/C Nanorod Array Electrocatalysts for ORR, OER, and Zn-Air Batteries. *Adv. Funct. Mater.* **2018**, *28*, 1704638. [[CrossRef](#)]
154. Liu, P.; Ran, J.; Xia, B.; Xi, S.; Gao, D.; Wang, J. Bifunctional Oxygen Electrocatalyst of Mesoporous Ni/NiO Nanosheets for Flexible Rechargeable Zn-Air Batteries. *Nanomicro. Lett.* **2020**, *12*, 68. [[CrossRef](#)] [[PubMed](#)]
155. Wang, F.; Zhao, H.; Ma, Y.; Yang, Y.; Li, B.; Cui, Y.; Guo, Z.; Wang, L. Core-shell-structured Co@Co₄N nanoparticles encapsulated into MnO-modified porous N-doping carbon nanocubes as bifunctional catalysts for rechargeable Zn—air batteries. *J. Energy Chem.* **2020**, *50*, 52–62. [[CrossRef](#)]
156. Wu, M.; Zhang, G.; Hu, Y.; Wang, J.; Sun, T.; Regier, T.; Qiao, J.; Sun, S. Graphitic-shell encapsulated FeNi alloy/nitride nanocrystals on biomass-derived N-doped carbon as an efficient electrocatalyst for rechargeable Zn-air battery. *Carbon Energy* **2020**, *3*, 176–187. [[CrossRef](#)]
157. Yu, J.; Li, B.; Zhao, C.; Liu, J.; Zhang, Q. Asymmetric Air Cathode Design for Enhanced Interfacial Electrocatalytic Reactions in High-Performance Zinc-Air Batteries. *Adv. Mater.* **2020**, *32*, e1908488. [[CrossRef](#)]
158. Fu, G.; Wang, J.; Chen, Y.; Liu, Y.; Tang, Y.; Goodenough, J.; Lee, J.-M. Exploring Indium-Based Ternary Thiospinel as Conceivable High-Potential Air-Cathode for Rechargeable Zn-Air Batteries. *Adv. Energy Mater.* **2018**, *8*, 1802263. [[CrossRef](#)]
159. Liu, W.; Zhang, J.; Bai, Z.; Jiang, G.; Li, M.; Feng, K.; Yang, L.; Ding, Y.; Yu, T.; Chen, Z.; et al. Controllable Urchin-Like NiCo₂S₄ Microsphere Synergized with Sulfur-Doped Graphene as Bifunctional Catalyst for Superior Rechargeable Zn-Air Battery. *Adv. Funct. Mater.* **2018**, *28*, 1706675. [[CrossRef](#)]
160. Pan, Z.; Chen, H.; Yang, J.; Ma, Y.; Zhang, Q.; Kou, Z.; Ding, X.; Pang, Y.; Zhang, L.; Gu, Q.; et al. CuCo₂S₄ Nanosheets@N-Doped Carbon Nanofibers by Sulfurization at Room Temperature as Bifunctional Electrocatalysts in Flexible Quasi-Solid-State Zn-Air Batteries. *Adv. Sci.* **2019**, *6*, 1900628. [[CrossRef](#)]
161. Balamurugan, J.; Nguyen, T.; Kim, D.; Kim, N.; Lee, J. 3D nickel molybdenum oxyselenide (Ni_{1-x}Mo_xOSe) nanoarchitectures as advanced multifunctional catalyst for Zn-air batteries and water splitting. *Appl. Catal. B Environ.* **2021**, *286*, 119909. [[CrossRef](#)]
162. Shi, X.; He, B.; Zhao, L.; Gong, Y.; Wang, R.; Wang, H. FeS₂–CoS₂ incorporated into nitrogen-doped carbon nanofibers to boost oxygen electrocatalysis for durable rechargeable Zn-air batteries. *J. Power Sources* **2020**, *482*, 228955. [[CrossRef](#)]
163. Wang, M.; Qian, T.; Zhou, J.; Yan, C. An Efficient Bifunctional Electrocatalyst for a Zinc-Air Battery Derived from Fe/N/C and Bimetallic Metal-Organic Framework Composites. *ACS Appl. Mater. Interfaces* **2017**, *9*, 5213–5221. [[CrossRef](#)]

164. Wei, W.; Shi, X.; Gao, P.; Wang, S.; Hu, W.; Zhao, X.; Ni, Y.; Xu, X.; Xu, Y.; Yan, W.; et al. Well-elaborated, mechanochemically synthesized Fe-TPP@ZIF precursors (Fe-TPP = tetraphenylporphine iron) to atomically dispersed iron–nitrogen species for oxygen reduction reaction and Zn-air batteries. *Nano Energy* **2018**, *52*, 29–37. [[CrossRef](#)]
165. He, Y.; Liu, X.; Yan, A.; Wan, H.; Chen, G.; Pan, J.; Zhang, N.; Qiu, T.; Ma, R.; Qiu, G. Hybrid Nanostructures of Bimetallic NiCo Nitride/N-Doped Reduced Graphene Oxide as Efficient Bifunctional Electrocatalysts for Rechargeable Zn–Air Batteries. *ACS Sustain. Chem. Eng.* **2019**, *7*, 19612–19620. [[CrossRef](#)]
166. Lin, C.; Li, X.; Shinde, S.; Kim, D.-H.; Song, X.; Zhang, H.; Lee, J.-H. Long-Life Rechargeable Zn Air Battery Based on Binary Metal Carbide Armored by Nitrogen-Doped Carbon. *ACS Appl. Energy Mater.* **2019**, *2*, 1747–1755. [[CrossRef](#)]
167. Wagh, N.; Shinde, S.; Lee, C.; Jung, J.-Y.; Kim, D.-H.; Kim, S.-H.; Lin, C.; Lee, S.; Lee, J.-H. Densely colonized isolated Cu-N single sites for efficient bifunctional electrocatalysts and rechargeable advanced Zn-air batteries. *Appl. Catal. B: Environ.* **2020**, *268*, 118746. [[CrossRef](#)]
168. Cai, J.; Zhang, X.; Yang, M.; Shi, Y.; Liu, W.; Lin, S. Constructing Co@WC_{1-x} heterostructure on N-doped carbon nanotubes as an efficient bifunctional electrocatalyst for zinc-air batteries. *J. Power Sources* **2020**, *485*, 229251. [[CrossRef](#)]
169. Li, Y.; Xu, K.; Zhang, Q.; Zheng, Z.; Li, S.; Zhao, Q.; Li, C.; Dong, C.; Mei, Z.; Pan, F.; et al. One-pot synthesis of FeN_xC as efficient catalyst for high-performance zinc-air battery. *J. Energy Chem.* **2022**, *66*, 100–106. [[CrossRef](#)]
170. Xu, W.; Lu, Z.; Zhang, T.; Zhong, Y.; Wu, Y.; Zhang, G.; Liu, J.; Wang, H.; Sun, X. An advanced zinc air battery with nanostructured superwetting electrodes. *Energy Storage Mater.* **2019**, *17*, 358–365. [[CrossRef](#)]
171. Zhao, J.; He, Y.; Chen, Z.; Zheng, X.; Han, X.; Rao, D.; Zhong, C.; Hu, W.; Deng, Y. Engineering the Surface Metal Active Sites of Nickel Cobalt Oxide Nanoplates toward Enhanced Oxygen Electrocatalysis for Zn-Air Battery. *ACS Appl. Mater. Interfaces* **2019**, *11*, 4915–4921. [[CrossRef](#)]
172. Majee, R.; Das, T.; Chakraborty, S.; Bhattacharyya, S. Shaping a Doped Perovskite Oxide with Measured Grain Boundary Defects to Catalyze Bifunctional Oxygen Activation for a Rechargeable Zn-Air Battery. *ACS Appl. Mater. Interfaces* **2020**, *12*, 40355–40363. [[CrossRef](#)]
173. Hong, J.; Kim, J.; Park, G.; Lee, J.; Lee, J.-K.; Kang, Y. A strategy for fabricating three-dimensional porous architecture comprising metal oxides/CNT as highly active and durable bifunctional oxygen electrocatalysts and their application in rechargeable Zn-air batteries. *Chem. Eng. J.* **2021**, *414*, 128815. [[CrossRef](#)]

Disclaimer/Publisher’s Note: The statements, opinions and data contained in all publications are solely those of the individual author(s) and contributor(s) and not of MDPI and/or the editor(s). MDPI and/or the editor(s) disclaim responsibility for any injury to people or property resulting from any ideas, methods, instructions or products referred to in the content.